Automatic Trajectory Planning for Low-Thrust Active Removal Mission in Low-Earth Orbit

Marilena Di Carlo, Juan Manuel Romero Martin, Massimiliano Vasile

Department of Mechanical and Aerospace Engineering, University of Strathclyde, 75 Montrose Street, Glasgow G1 1XJ, United Kingdom

Abstract

In this paper two strategies are proposed to de-orbit up to 10 non-cooperative objects per year from the region within 800 and 1400 km altitude in Low Earth Orbit (LEO). The underlying idea is to use a single servicing spacecraft to de-orbit several objects applying two different approaches. The first strategy is analogous to the Traveling Salesman Problem: the servicing spacecraft rendezvous with multiple objects in order to physically attach a de-orbiting kit that reduces the perigee of the orbit. The second strategy is analogous to the Vehicle Routing Problem: the servicing spacecraft rendezvous and docks with an object, spirals it down to a lower altitude orbit, undocks, and then spirals up to the next target.

In order to maximise the number of de-orbited objects with minimum propellant consumption, an optimal sequence of targets is identified using a bio-inspired incremental automatic planning and scheduling discrete optimisation algorithm. The optimisation of the resulting sequence is realised using a direct transcription method based on an asymptotic analytical solution of the perturbed Keplerian motion. The analytical model takes into account the perturbations deriving from the J_2 gravitational effect and the atmospheric drag.

Keywords: Active Debris Removal; Orbital Debris; Debris Mitigation; Automated Trajectory Design; Automatic Planning and Scheduling; Low-Thrust Transfers

Email address: juan.romero-martin@strath.ac.uk, marilena.di-carlo@strath.ac.uk, massimiliano.vasile@strath.ac.uk (Marilena Di Carlo, Juan Manuel Romero Martin, Massimiliano Vasile)

1. Introduction

Since the beginning of the space era, humankind have put into orbit over 10,000 objects (Rossi & Valsecchi, 2006). Only 6% of these are active satellite while the rest are space debris (Rossi & Valsecchi, 2006). The growth of space debris population represents a collision threat for satellite and manned spacecraft in Earth orbit. Recent studies have concluded that regions within Low Earth Orbit (LEO) have already reached a critical density of objects which will eventually lead to a cascading process known as the Kessler syndrome (Kessler et al., 2010). It is expected for the LEO debris population to increase by approximately 30% in the next 200 years (Rossi & Valsecchi, 2006; Hildreth et al., 2014). The Inter-Agency Space Debris Coordination Committee has issued guidelines to mitigate the growth of space debris (IADC et al., 2007). However it has been proven that compliance with these recommendations will not stop the exponential growth. Liou & Johnson (2008) have indeed proved that, under the assumption that no spacecrafts are launched after December 2005, the debris population would still grow, driven by collision in the 900-1000 km altitude range. The active removal of five to ten large objects per year is required to stabilise the population (Liou & Johnson, 2008). Since in a no-further-release scenario collisions are the only reason for the growth of debris population, and since collision probability is a function of the object's cross section area, large objects are the main candidates for active removal (Virgili & Krag (2009)). Different methods have been proposed for removal of debris in LEO. These methods can be contact-less method, such as the Ion-Beam Shepherd (Bombardelli & Pelaez, 2011), lasers and solar concentrator (Vasile et al., 2010), or based on a physical contact with the spacecraft using throw-net, harpoon (Wormnes et al., 2013), clap or robotic arm. Mainly, the objective of the contact methods is to bring the space debris into a disposal or a re-entry orbit together with the servicing spacecraft. However, the robotic arm method can be used to attach a de-orbit device on the space debris, and then, the disposal of the debris will be performed in a controlled manner using this de-orbit kit (Kumar et al., 2015).

Different scenarios for the active removal of space debris have been proposed in the literature. Castronuovo (2011) presents a mission for the removal of debris from Sun-synchronous orbit. A servicing spacecraft carrying

a number of de-orbiting devices is used to remove 35 objects from this region in 7 years. The spacecraft uses chemical propellant and is serviced 7 times during the mission time in order to be resupplied with propellant and more de-orbiting devices. Braun et al. (2013) present a study in which different scenarios are considered for chemical or electric propelled servicing spacecraft and for the use of de-orbit kits device or direct transfer of the objects on a disposal orbit. The targets are identified using a priority criterion based on the probability of a catastrophic collision and on the objects' masses. The sequence of targets to be removed is then computed using a brute-force approach in which each possible permutation is simulated. Peterson (2012) identifies desirable targets based upon the probabilistic likelihood of objects contributing to the debris field. Both an impulsive and a low thrust missions are studied, with a limit total available ΔV assigned to them. ΔV analysis for transfer between object is mainly based on the change in the right ascension of the ascending node and no optimisation or identification of target sequence is performed. Stuart et al. (2015) present an automated procedure to generate route plans for an active debris removal campaign based on Ant Colony Optimization (ACO) combined with auction and bidding processes. The heuristic of the ACO is similar to the Physarum algorithm presented in this paper. Stuart formulates the problem as a typical multi-vehicle routing problem (MVRP) employing ACO to create preliminary encounter tours and to determine the total number of spacecrafts required to complete mitigation tasks. Auction and bidding process are used to coordinate the operation of the debris-mitigating satellites for both pre-mission planning and real-time adjustments to baseline designs. Finally Olympio & Frouvelle (2014) consider space debris on Sun-synchronous orbits. A Lambert's problem with J2 perturbation is used to compute the cost of all the debris-to-debris transfers and a branch-and-prune algorithm is used to construct the target sequence. The transfers between objects in the sequence is then optimised using an indirect method for the low-thrust transfers. The considered propulsion system has a thrust amplitude ranging from 0.5 N to 10 N for a 1000 kg spacecraft.

This paper starts from previous work by the authors Zuiani & Vasile (2012) on the multi-objective optimisation of de-orbiting sequences for expended satellites and proposes two strategies to automatically plan active debris removal missions in which a single servicing spacecraft, equipped with an electric engine, removes multiple objects from LEO. The underlying optimal control problem defining the transfer between pairs of objects is solved with a recently developed approach based on asymptotic analytical solutions of the

Keplerian motion under constant acceleration and using surrogate models for the evaluation of the cost of the transfer in order to reduce the computational burden of the combinatorial algorithm.

The paper starts with a description of the considered ADR strategies in Sec. 2; then the targets selection method used is addressed in Sec. 3. The discrete decision making algorithm for the object sequence selection and the low-thrust transfer model are described in Sec. 4 and 5. The obtained results are presented in Sec. 7, and some final remarks conclude the paper.

2. Active debris removal strategies

In this paper, two strategies to actively remove objects from LEO are proposed and studied. These two strategies are here called the Deorbiting Traveling Salesman Problem (TSP) and the Deorbiting Vehicle Routing Problem (VRP).

The Deorbiting TSP is analogous to the classic Traveling Salesman Problem: a servicing spacecraft (chaser) rendezvous with multiple objects (targets) in order to physically attach a de-orbiting system that reduces the altitude of the perigee of the orbit of the target down to 300 km.

The Deorbiting VRP is analogous to the classic Vehicle Routing Problem: a servicing spacecraft rendezvous with an object, grabs it and spirals down to a circular disposal orbit with an altitude of 300 km. Once this orbit is reached, the chaser disengages with the target and moves to the next target. The disposal orbit can be seen as the depot of a typical VRP.

Fig. 1 illustrates the different mission phases of the two proposed strategies.

3. Target selection

A catalog of the current objects in LEO is regularly maintained by the North American Aerospace Defence Command (NORAD). Each object in the catalog is identified by its Two-Line Elements (TLE) set, defining its orbital parameters at a given epoch. For this work, TLE of all objects characterized by perigee altitude $h_p \geq 800$ km and apogee altitude $h_a \leq 1400$ km are taken from *space-track.org*. In order to target objects more likely to cause collision, only TLE characterized by Radar Cross Section (RCS) > 1 are considered.

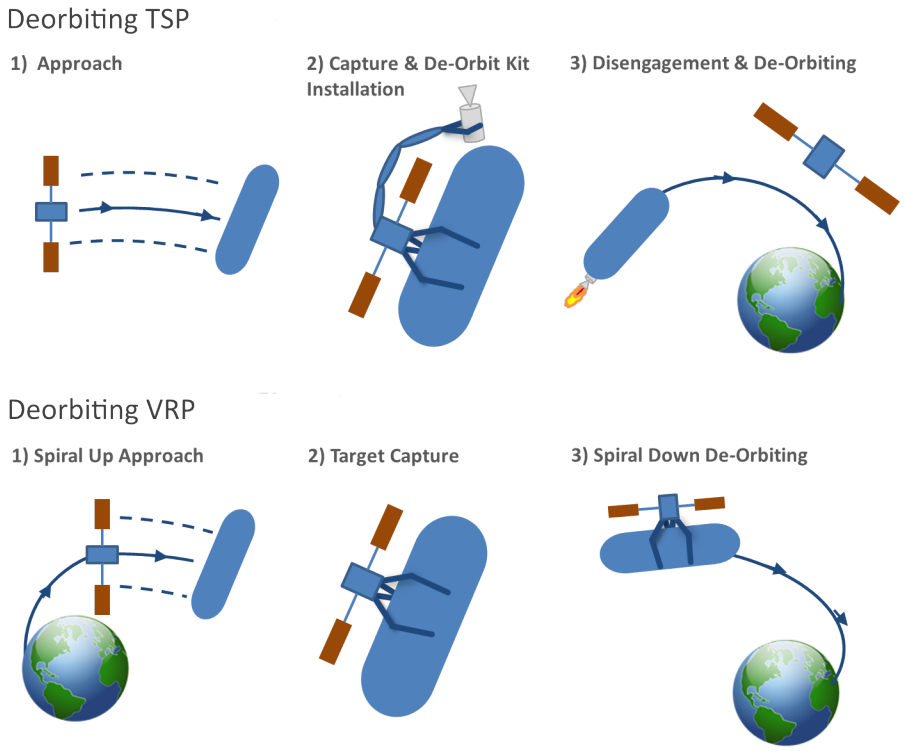

Figure 1: Mission phases of the two studied ADR strategies.

The Radar Cross Section is a measure of how detectable is an object with a radar; object with RCS > 1 are classified as large. Up to 721 objects characterized by $h_p \geq 800$ km, $h_a \leq 1400$ and RCS > 1 are found; their distribution in term of semimajor axis vs. inclination and semimajor axis vs. right ascension of the ascending node, Ω, is shown in Fig. 2.

The potential 721 target objects are then further selected based on two main criteria: the right ascension of the ascending node drift due to the second zonal harmonic of the gravity J_2 and the Criticality of Spacecraft Index (CSI) (Rossi et al., 2015). Fig. 2 shows that Ω is widely spread. Low-thrust maneuvers to change the right ascension are particularly expensive and require long time when compared to maneuvers to change other orbital elements. Ruggiero et al. showed that changing 1 degree of right ascension requires 10 days when using optimal thrust angle for the change of Ω (Ruggiero et al., 2011). In this paper the change of Ω is performed by taking

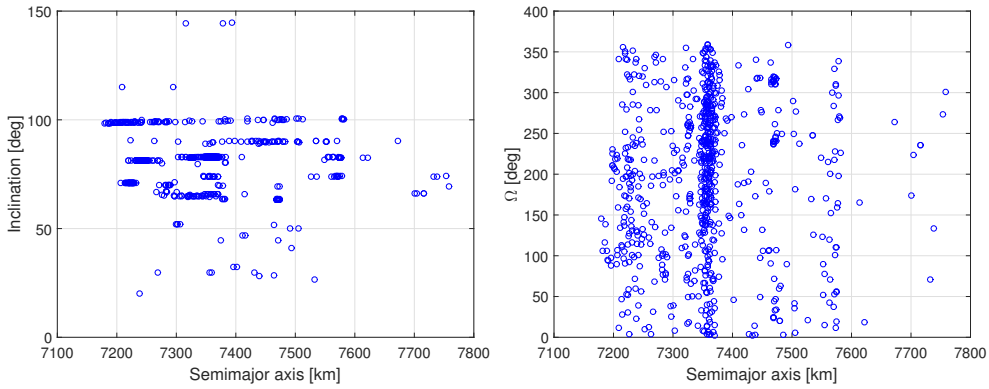

Figure 2: Semimajor axis, inclination and right ascension of objects in LEO characterized by $h_p \geq 800$ km, $h_a \leq 1400$ and RCS$\geq$1.

advantage of the natural rate of nodal regression due to J_2 and its dependence on altitude. Transferring the spacecraft to lower or higher altitude changes the rate of Ω relative to the initial orbit so that a shift in Ω can be realised (Pollard, 2000). The variation of Ω of the servicing spacecraft depends on its altitude and inclination i according to (Vallado & McClain, 2001):

$$\dot{\Omega} = -\frac{3}{2} n J_2 \left(\frac{R_\oplus}{a(1-e^2)} \right)^2 \cos i \tag{1}$$

where n is the orbit's mean motion, $R_\oplus$ the mean Earth's radius and a and e are the orbit's semimajor axis and eccentricity. The effect of a change of semimajor axis on the variation of Ω is greater when the inclination is smaller, because of the $\cos i$ term in the Eq. (1).

A further classification of objects with low inclination is realised based on the Criticality of Spacecraft Index (CSI). The Criticality of Spacecraft Index expresses the environmental criticality of objects in Low Earth Orbit taking into account the physical characteristics of a given object, its orbit and the environment where this is located (Rossi et al., 2015). We did not compute the CSI for the object we selected but we compared their location, in the inclination-perigee/apogee space, against the location, in the same space, of the most critical objects reported in the work of (Rossi et al., 2015). Fig. 3 shows the perigee and the apogee altitudes of the 721 objects characterized by $h_p > 800$ km and $h_a <$1400 km as a function of the inclination. It can be compared with Figure 8 in Rossi et al. (2015) to see that the 25 circled

objects in Fig. 3 are in the same region as the 100 most critical objects in terms of CSI. These 25 objects are the ones selected for this study. Their orbital elements at epoch $t_0 = 30$ May 2015 are reported in Table 1 and shown in Fig. 4.

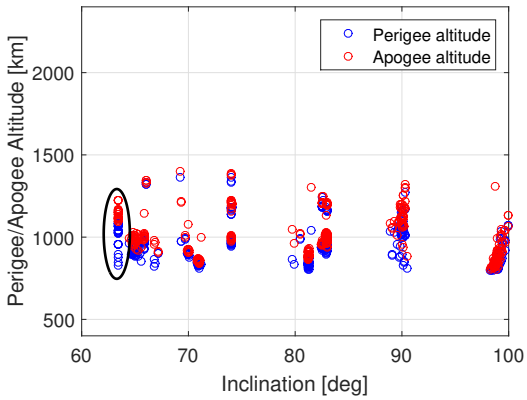

Figure 3: Perigee and apogee altitude of objects in LEO with $h_p > 800$ km, $h_a < 1400$ and RCS>1.

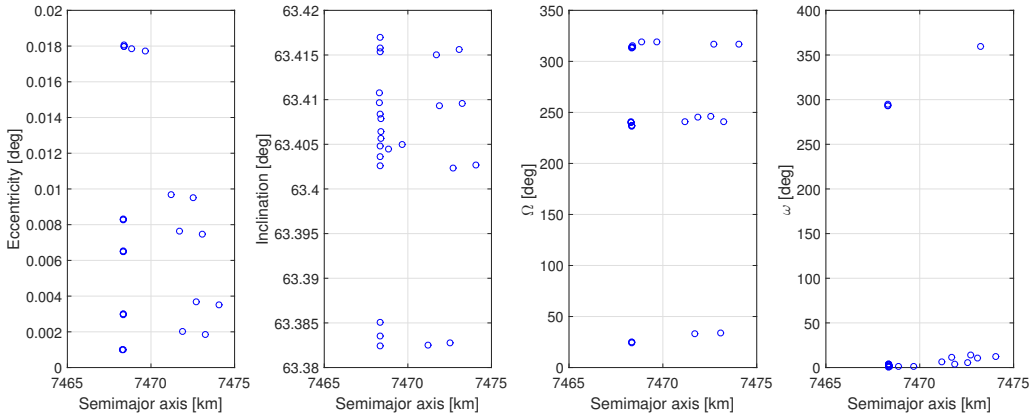

Figure 4: Orbital elements of the selected objects.

Table 1: List of selected objects.

	ID	a [km]	e	i [deg]	Ω [deg]	ω [deg]	E [deg]
1	39012	7468.3502	0.0083	63.3824	237.3044	0.8990	359.2169
2	39016	7471.1909	0.0097	63.3825	240.6863	6.5523	353.6732
3	39015	7472.5431	0.0095	63.3828	246.1591	5.6338	354.5722
4	39011	7468.3501	0.0083	63.3835	237.2911	0.9268	359.1897
5	39013	7468.3457	0.0083	63.3851	236.4881	0.7138	359.3978
6	40113	7472.7134	0.0037	63.4023	316.5715	13.7191	346.4819
7	40110	7468.3365	0.0030	63.4026	313.7710	3.4835	356.6392
8	40114	7474.0679	0.0035	63.4027	317.0490	12.1346	348.0508
9	40111	7468.3378	0.0030	63.4036	313.9539	3.3535	356.7684
10	36417	7468.8627	0.0178	63.4045	319.3205	1.2414	136.7021
11	40109	7468.3382	0.0030	63.4048	313.0739	3.0576	357.0626
12	36418	7469.6579	0.0177	63.4050	318.8647	0.8968	90.3057
13	36415	7468.3664	0.0181	63.4057	313.6971	1.5540	358.6008
14	36413	7468.3637	0.0180	63.4064	315.3091	1.5248	358.6278
15	36414	7468.3642	0.0180	63.4079	313.8604	1.2339	358.9091
16	40340	7468.3186	0.0010	63.4084	240.6788	293.4985	66.5005
17	40343	7471.8760	0.0020	63.4093	245.3040	3.4906	356.6256
18	40342	7473.2452	0.0019	63.4096	240.8979	359.1859	0.9133
19	40339	7468.3132	0.0010	63.4097	239.8082	294.9368	65.0721
20	40338	7468.3152	0.0010	63.4108	239.8075	293.4250	66.5729
21	39243	7471.6919	0.0076	63.4150	32.8672	11.6594	348.6165
22	39240	7468.3470	0.0065	63.4154	24.7900	3.7401	356.4085
23	39244	7473.0697	0.0075	63.4156	33.7082	10.7899	349.4691
24	39239	7468.3482	0.0065	63.4158	24.7599	3.6762	356.4729
25	39241	7468.3452	0.0065	63.4170	23.8973	3.3104	356.8339

4. Incremental planning and scheduling algorithm

The automatic planning and scheduling algorithm used in this paper is based on a single objective discrete optimisation algorithm which takes inspiration from the biology of the single cell slime mold Physarum Polycephalum. The Physarum Polycephalum organism has been endowed by nature with a simple but powerful heuristic that can solve complex discrete decision making problems (Nakagaki et al., 2000; Adamatzky et al., 2011; Hickey et al., 2008; Tero et al., 2006, 2008). In its main vegetative state, *plasmodium* state, the

Physarum Polycephalum forms a network of veins called *pseudopodia*. This network of veins spreads searching for food sources evolving and reshaping with time to find the optimal shape that optimises the energy required to feed the organism (Tero et al., 2008). The flux on the veins varies depending on the distance between the food source and the center of the Physarum. For example, the shortest is the path, the largest is the flux and viceversa.

The Physarum algorithm works modeling the discrete decision making problems into a decision graphs were nodes represent the possible decisions while arcs represent the cost vector associated with decisions. The mechanism of Physarym is analogous to the most commonly known Ant Colony Optimisation algorithm (Hickey et al., 2008). The decision graph is incrementally grown or explored by Virtual Agents using the Physarum-based heuristic. Unlike branch and prune algorithms, that use a set of deterministic branching and pruning heuristics, the Physarum algorithm uses probabilistic heuristics to decide to branch or prune a vein. To be more specific, branches are never really pruned but the probability of selecting them falls to almost zero. The Physarum algorithm has already been tested on a variety of combinatorial problems with good results (Adamatzky et al., 2011; Masi & Vasile, 2014; Romero et al., 2014)

In order to apply the Physarum algorithm, the problem is modeled using a tree-like topology. Starting from a dummy node, that represents the root node, each following children nodes of the root node represent the first servicing task, and its children represent the successive servicing tasks. The decision graph is incrementally grown with time by the virtual agents using the Physarum-based heuristic. Each current node becomes the parent of the following children until an end condition is reached and one full solution is generated. Each arc connecting a parent with a child has an associated cost, evaluated making use of the models presented in Sec. 5.

The two ADR strategies studied in this paper have different stopping conditions. When the planning algorithm reaches the stopping condition a full solution is produced. For the Deorbiting TSP, the stopping condition is obtained when the maximum mission time T_{max} is reached or when the number of installed de-orbit kits reaches the value N_{Kits}. N_{Kits} represents the number of kits that can be stored on-board the chaser. For the Deorbiting VRP, the stopping condition is reached when the total mission time is equal to T_{max}.

In this section a brief description of the Physarum's mathematical model is presented; for more details on Physarum algoirthm the interested reader

can refer to Vasile & Becerra (2014). Note that, in this work, the Physarum algorithm was implemented in its unidirectional version. The mathematical model of Physarum consists mainly of two parts: the decision network exploration and decision network growth. The main parameters of the Physarum solver are summarised in Table 2 and the complete pseudocode is provided in Algorithm 1.

Table 2: Main setting parameters for the Physarum solver.

m	Linear dilation coefficient, see Eq. (3)
ρ	Evaporation coefficient, see Eq. (4)
GF	Growth factor
N_{agents}	Number of virtual agents
$N_{Generation}$	Number of generations
p_{ram}	Probability of ramification
r_{ini}	Initial vein's radius
λ	Weight on ramification, see Eq. (6)

4.1. Decision network exploration

The decision network exploration is based on the flux through the network of Physarum veins. The flux of the Physarum veins can be modelled as a classical Hagen-Poiseuille flow in cylindrical ducts with variable diameter that varies with time (Hickey et al., 2008; Tero et al., 2006, 2008):

$$Q_{ij} = \frac{\pi r_{ij}^4}{8\mu} \frac{\Delta p_{ij}}{L_{ij}} \tag{2}$$

where Q_{ij} is the flux between i and j, μ is the dynamic viscosity, r_{ij} is the radius of the vein, L_{ij} is the length of the vein, and Δp_{ij} is the pressure gradient. In this paper, L_{ij} is substituted by the cost of the transfer between two subsequent targets, ΔV. For a better understanding of these parameters, they have been illustrated by means of a simple graph in Fig. 5.

The variation of the flux through the veins occurs due to the change with time of the radii of the veins. These changes are produced mainly by two processes: dilation and contraction of the veins. The dilation of the veins is caused by the increment of the flowing nutrients throughout a vein. The dilation process can be modelled using a monotonic function of the flux:

Algorithm 1 Incremental Physarum Solver

initialize m, ρ, GF, N_{agents}, p_{ram}, λ
for each generation **do**
  for each virtual agent **do**
    if $EndConditoin = true$ **then**
      Create a new full solution from the current node
      Continue
    end if
    if $\nu \in \mathcal{U}(0,1) \leq p_{ram}$ **then**
      Using Eq. (6) create a new decision path, building missing links and nodes
    else
      Move on existing graph using Eq. (5).
    end if
  end for
  Contract and dilate veins using Eqs. (3), (4)
  if r_{ij} exceeds upper radius limit **then**
    Block radius increment
  end if
  Update fluxes and probabilities using Eqs. (2), (5)
  if *restart condition* **then**
    Update veins' radii
    Update fluxes and probabilities using Eqs. (2), (5)
  end if
end for

$$\left.\frac{d}{dt} r_{ij}\right|_{dilation} = f\left(Q_{ij}\right) \tag{3}$$

On the other hand, the contraction of the veins is caused by an evaporation effect and can be modelled as linear function of the radius:

$$\left.\frac{d}{dt} r_{ij}\right|_{contraction} = -\rho r_{ij} \tag{4}$$

where $\rho \in [0,1]$ is a pre-defined evaporation coefficient. Then, the probability associated with each vein connecting the node i and the node j can

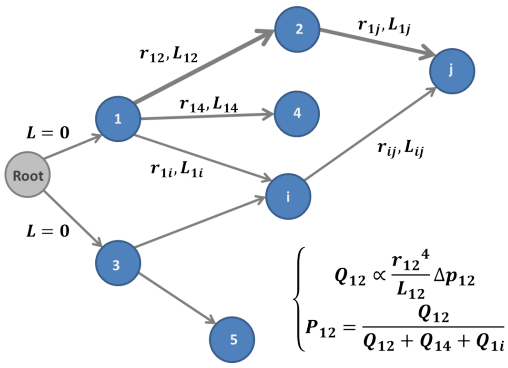

Figure 5: Physarum solver decision network; thicker arrows represent higher fluxes. In this example $Q_{12} > Q_{14} \rightarrow P_{12} > P_{14}$

be computed using a simple adjacency probability matrix based on fluxes as follow:

$$P_{ij} = \begin{cases} \frac{Q_{ij}}{\sum_{j \in N_i} Q_{ij}} & if\ j \in N_i \\ 0 & if\ j \notin N_i \end{cases} \tag{5}$$

where N_i is the set of neighbouring veins to a node i.

4.2. Growth of the decision network

The incremental growth of the decision network is based on a weighted roulette. At every node of the tree, each virtual agent can generate a new branch or move along an existing one. At each node, the virtual agent has a probability p_{ram} of ramification towards new nodes that are not yet linked with the current one. On line 5 of Algorithm 1, a random number v is drawn from a uniform distribution $U(0, 1)$ and the condition $v < p_{ram}$ is verified. Assuming that the agent is at node i, if ramification is the choice, the virtual agent evaluates the set of possible new branches and assigns a probability p_{ij} of constructing a new link from the current node i to a new possible node $j \in \bar{N}_i$, where $\bar{N}_i$ is the set of unlinked nodes (for example nodes 3 and 4 in Fig. 6), according to:

$$p_{ij} \propto \frac{1}{L_{ij}^{\lambda}} \tag{6}$$

where λ is a pre-defined weight exponent. Fig. 6 illustrates the concept of possible ramification where dotted lines represent feasible branches not yet existing. If a virtual agent is at node 1, it has a probability p_{ram} of

ramification towards the unlinked nodes 3 and 4. If the virtual agent decides to create a new link, a new node is selected according to Eq. (6) (line 6 of Algorithm 1).

If a set of linked nodes is available, the virtual agent can decide, with probability $(1-p_{ram})$, to traverse the existing branches in the neighbourhood N_i (line 8 of Algorithm 1). In the case illustrated in Fig. 6 when virtual agent is at node 1, it can explore the already linked nodes 2 or create new links to the unlinked nodes 3 and 4.

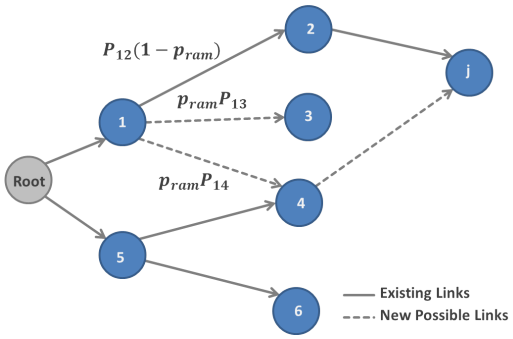

Figure 6: Illustration of the ramification towards a new node.

4.3. Problem formulation

As introduced in Sec. 2, the two proposed ADR strategies are analogous to the typical TSP and VRP. In the TSP the goal is to minimise the total path length to visit every town/node once and only once. In the Deorbiting analogous, the goal is to minimise the total ΔV to execute all servicing tasks only one. In contrast to the regular TSP, where the cost of each arc connecting two nodes is constant, in the ADR case, the cost of the arc depends on the mass of the chaser, which varies with time. In fact, the mass of the servicing spacecraft depends on the propellant mass, that is progressively consumed to rendezvous with all the satellites, and on the number of de-orbit kits, that are progressively used to perform de-orbiting. The ADR analogous has other key distinctive features:

- Only n_T tasks among S_s are performed, where S_s is the set of targets to be serviced. n_T depends on the number of de-orbit kits available on-board the chaser.
- There is a constraints on the transfers time (ToF) between tasks so that $ToF \in [ToF_{min}, ToF_{max}]$.

- There is a waiting time at each target. This waiting time is the time required to performed the servicing, $t_{servicing}$.

The Deorbiting VRP is equivalent to the classic VRP, where after each service, the vehicle (the chaser in our case) has to return to the depot (the disposal orbit) before proceeding to the next service. Similar to the TSP, the goal of the VRP is to minimise the total distance covered and to conduct every task once and only once. The following features have been added to the ADR analogous:

- There is a global duration constrain on the total mission time, $t_{mission} < T_{max}$.
- There is a local duration constrain on the transfers time between tasks so that $ToF \in [ToF_{min}, ToF_{max}]$.

As stated previously in this section, the decision graph is incrementally grown by the virtual agents where each node of the graph represents a decision. Each of the nodes are connected by arcs, and these arcs have an associated cost, evaluated making use of the model presented in Sec. 5. This cost is the ΔV associated to the transfer between targets. In the Physarum algorithm, the variable L_{ij} in Eqs (2) and (6) is replaced by ΔV.

Both for the TSP and VRP problems, the Physarum algorithm evaluate the cost of the low-thrust transfer between satellites using a surrogate model, rather than the actual low-thrust model. This is justified by the combinatorial complexity of the problem and by the computational time required by the computation of the low-thrust transfer. To justify this method, an estimation of the total number of required operations and of the corresponding computational time, using the low-thrust model, is given in the following. Considering the set of 25 possible targets, the number of combinations of target-to-target transfer arcs can be computed using the formula $n!/(n-k)!$, where n=25 and k is the number of objects of the subset. In this case $k = 2$, giving a total number of 600 different transfer arcs. Considering a time of flight for the transfer from 1 to 180 days and a time step of 0.25 days, the total number of possible time of flights for each transfer arc is 716. Therefore, the total number of transfer arcs that should be computed is 600*716 = 429600. Hence, assuming that the low-thrust solver takes on average 25 sec to compute a transfer arc on an Intel(R) Core(TM) i7-3770 CPU 3.4GHz and 8GB RAM, the total computational time required to perform an exhaustive assessment of the search space is approximately 1243 days. Therefore,

in order to reduce the computational time required by the Physarum in the evaluation of the cost of the transfer arcs, a surrogate model of the low-thrust transfers is used (Sec. 5.6.1). The evaluation of the surrogate model has an almost instantaneous computational time cost, resulting in a considerable reduction on the computational time.

5. Low-thrust transfer model

In this section the method used to compute the ΔV required to assess the cost of the transfer for the Deorbiting TSP and the Deorbiting VRP is described.

5.1. Debris dynamical model

In this work, the mean elements at epoch t_0 of each target are taken from the TLE catalog (Hoots et al., 1980) and are propagated forward in time considering only the J_2 effect, since drag is not relevant at the considered altitude. The effect of drag is neglected also for the transfer between two targets in the Deorbiting TSP but is taken into account in the deorbiting and orbit raising of the Deorbiting VRP. Neglecting the atmospheric drag for the propagation of the orbits of the target objects is justified by the small variations of a and e, due to drag, over a time interval of two years (Fig. 7).

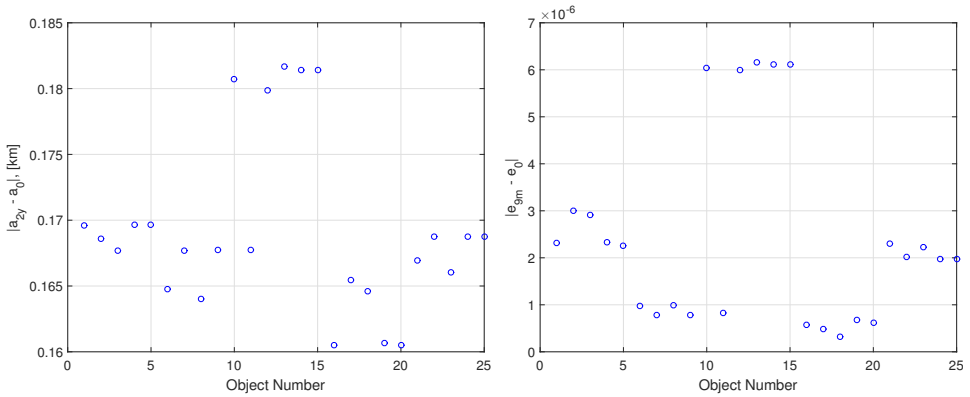

Figure 7: Variation of semimajor axis and eccentricity of the target objects during a time period of two years.

For each possible target, therefore, a, e and i are assumed to be constant,

while Ω and ω change according to (Vallado & McClain (2001)):

$$\Omega(t) = \Omega(t_0) - \frac{3}{2}\bar{n}J_2\left(\frac{R_\oplus}{p}\right)^2 \cos i(t - t_0) \tag{7}$$

$$\omega(t) = \omega(t_0) + \frac{3}{2}\bar{n}J_2\left(2 - \frac{5}{2}\sin^2 i\right)^2 (t - t_0) \tag{8}$$

where

$$\bar{n} = n\left[1 + \frac{3}{2}J_2\left(\frac{R_\oplus}{p}\right)^2 \sqrt{1 - e^2}\left(1 - \frac{3}{2}\sin^2 i\right)\right] \tag{9}$$

5.2. Time independence of the transfers

The rate of change of Ω and ω due to J_2 is different for each selected target object and depends on their orbital elements. During the transfer from any object A to any object B, realised in a time of flight ToF, the chaser has to correct Ω and ω by an amount:

$$\Delta\Omega(t_0, ToF) = \Omega_B(t_0 + ToF) - \Omega_A(t_0) \tag{10}$$

$$\Delta\omega(t_0, ToF) = \omega_B(t_0 + ToF) - \omega_A(t_0) \tag{11}$$

The different rates of change of Ω and ω for the two objects A and B result in different values of $\Delta\Omega$ and $\Delta\omega$ when transferring from one object to another at different epochs. This means that, for $t_1 \neq t_0$:

$$\Delta\Omega(t_0, ToF) \neq \Delta\Omega(t_1, ToF) \tag{12}$$

and

$$\Delta\omega(t_0, ToF) \neq \Delta\omega(t_1, ToF) \tag{13}$$

As a consequence, transfers realised at different starting epochs would be characterised by different ΔV's. Consider now each combination of two objects A and B and the quantities:

$$\Delta\Omega_{AB}(t_0, T_{1y}) = [\Omega_A(t_0 + T_{1y}) - \Omega_B(t_0 + T_{1y})] - [\Omega_A(t_0) - \Omega_B(t_0)] \tag{14}$$

$$\Delta\omega_{AB}(t_0, T_{1y}) = [\omega_A(t_0 + T_{1y}) - \omega_B(t_0 + T_{1y})] - [\omega_A(t_0) - \omega_B(t_0)] \tag{15}$$

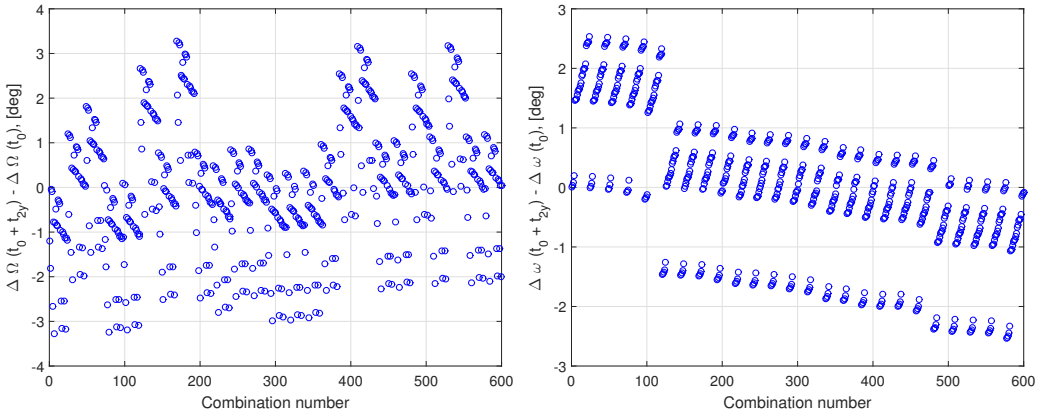

Figure 8: $\Delta\Omega_{AB}(t_0, T_{1y})$ and $\Delta\omega_{AB}(t_0, T_{1y})$ for the 600 combinations of transfers resulting from the 25 selected objects.

where t_0 is a given epoch and $T_{1y} = 1$ year. The quantities in Eqs. 14 and 15 are shown in Fig. 8 for all the 600 combinations of transfers resulting from the 25 selected objects.

Figures 8 show that the differences in $\Delta\Omega$ are limited to less than 3.28 deg over one year and those of ω are limited to less than 2.53 degrees over the same period of time. Using the transfer model described in Sec. 5.3, the ΔV required to realise the following two transfers can be computed:

- $a_A = 7470$ km $\rightarrow a_B = a_A$
- $e_A = 0 \rightarrow e_B = e_A$
- $i_A = 63$ deg $\rightarrow i_B = i_A$
- $\Omega_A(t_0) \rightarrow \Omega_B(t_0 + ToF)$

and

- $a_A = 7470$ km $\rightarrow a_B = a_A$
- $e_A = 0 \rightarrow e_B = e_A$
- $i_A = 63$ deg $\rightarrow i_B = i_A$
- $\Omega_A(t_0 + T_{1y}) \rightarrow \Omega_B(t_0 + T_{1y} + ToF)$

The worst possible transfer was considered, that is the one corresponding to:

$$[\Omega_B(t_0 + T_{1y}) - \Omega_A(t_0 + T_{1y})] - [\Omega_B(t_0) - \Omega_A(t_0)] = 3.28 \text{ deg} \tag{16}$$

Fig. 9 shows the difference between the ΔV's required to realise the two transfers defined here above. The difference in ΔV is plotted against the ToF. The difference in the ΔV's required to realise transfers with different

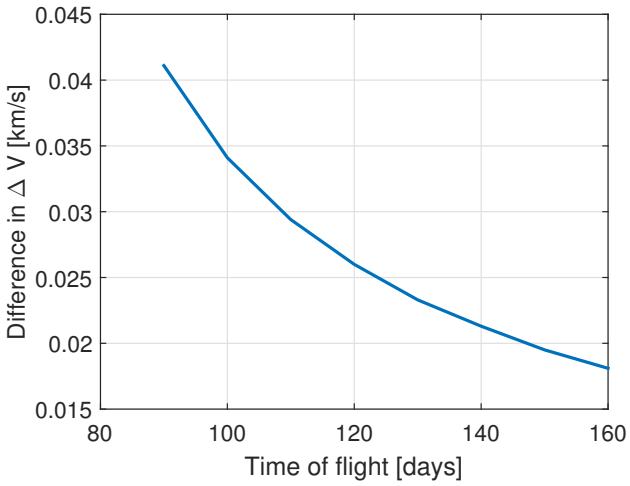

Figure 9: Difference in Δ for transfers computed at different epochs (t_0 or $t_0 + T_{1y}$.

values of $\Delta\omega$ are expected to be lower than those in Fig. 7 given the smaller values of the difference in $\Delta\omega$. Given the result in Fig. 9 the time independence assumption was applied to the calculation of all the transfers in the remainder of this paper. This assumption allows one to represent the ΔV only as a function the mass of the target and the ToF (see Sec. 5.6.1).

5.3. Transfer model

The state $\mathbf{X}$ of the spacecraft is modeled using non-singular equinoctial elements (Battin, 1999):

$$\mathbf{X} = \begin{cases} a \\ P_1 = e \sin(\Omega + \omega) \\ P_2 = e \cos(\Omega + \omega) \\ Q_1 = \tan \frac{i}{2} \sin \Omega \\ Q_2 = \tan \frac{i}{2} \cos \Omega \\ L = \Omega + \omega + \theta \end{cases} \tag{17}$$

In the previous expressions L is the true longitude and θ represents the true anomaly. The transfers between objects are optimised in order to reduce the total propellant consumption, or ΔV. The acceleration $\mathbf{a}_{LT}$ exerted by the thruster on the spacecraft is expressed in the spacecraft body-fixed radial-transverse-normal reference frame as (Zuiani & Vasile (2015)):

$$\mathbf{a}_{LT} = \begin{cases} a_r = \varepsilon \cos \beta \cos \alpha \\ a_\theta = \varepsilon \cos \beta \sin \alpha \\ a_h = \varepsilon \sin \beta \end{cases} \tag{18}$$

where ε is the acceleration magnitude, α is the in-plane azimuth angle and β is the out-of-plane elevation angle.

Each orbit revolution of the servicing spacecraft is divided into four sectors: two thrust arcs (at perigee and apogee) and two coast arcs. During each thrust arc the value of α and β are kept constant. In order to consider situations in which thrusting at perigee and apogee could not be the optimal choice, an additional decision parameter that produces a shift along the orbit of the center of the perigee thrust is introduced. The control variables to optimise are, therefore:

- dL_p, amplitude of the perigee thrust arc;
- α_p, azimuth angle of the thrust vector during the perigee thrust arc;
- β_p, elevation angle of the thrust vector during the perigee thrust arc;
- η, angle defining the shift of the first thrust arc (perigee thrust arc) with respect to the perigee;
- dL_a, amplitude of the apogee thrust arc;
- α_a, azimuth angle of the thrust vector during the apogee thrust arc;
- β_a, elevation angle of the thrust vector during the apogee thrust arc.

On each thrust arc, the state of the servicing spacecraft is propagated using an averaged analytical solution of the perturbed Keplerian motion. The averaged analytical propagator is based on a set of analytical formulae to propagate the perturbed Keplerian motion over a complete revolution; the averaged orbital elements variations $\dot{\mathbf{X}}$ are then numerically propagated, as it is done in classical semi-analytical techniques (Cefola et al., 1974):

$$\bar{\mathbf{X}}(t) = \mathbf{X}_0 + \int_{t_0}^{t} \dot{\mathbf{X}} \left(\tau, \bar{\mathbf{X}}(\tau), dL_p(\tau), \alpha_p(\tau), \beta_p(\tau), dL_a(\tau), \alpha_a(\tau), \beta_a(\tau), \eta(\tau)\right) d\tau \tag{19}$$

$\bar{\mathbf{X}}$ is the vector of averaged orbital elements and $\dot{\mathbf{X}}$ is computed using:

$$\dot{\mathbf{X}} = \frac{\mathbf{X}_{2\pi} - \mathbf{X}_0}{T} \tag{20}$$

where T is the orbital period. The contribution of the J_2 zonal harmonic was already included in the analytical formulae developed in (Zuiani & Vasile, 2015). However, the Deorbiting VRP strategy requires also the effect of the atmospheric drag. An analytical solution for the effect of the atmospheric drag will be developed in the next section.

5.3.1. Perturbation due to atmospheric drag

In Zuiani & Vasile (2015) analytical expressions for the motion of a spacecraft under a perturbing acceleration were derived using an asymptotic expansion of Gauss' equations in terms of non-singular equinoctial elements. The perturbing accelerations were expressed in a radial-transverse-normal reference frame, as in Eq. (18). The first step towards the derivation of an analytical formula for the effect of drag is to express drag in this reference frame as a function of the non-singular equinoctial elements. The magnitude of the acceleration due to drag can be defined as (Vallado & McClain, 2001):

$$a_D = \frac{1}{2}\rho C_D \frac{A}{m} v^2 \tag{21}$$

where ρ is the atmospheric density, C_D the drag coefficient of the spacecraft, A the area of the spacecraft in the direction of the velocity, m the mass and v its velocity. It is possible to express a_D as a function of the equinoctial elements by using the energy equation to write the square of the velocity as:

$$v^2 = \frac{\mu}{a}\left(\frac{2\Phi(L)}{B^2} - 1\right) \tag{22}$$

where $\Phi(L) = 1 + P_1 \sin L + P_2 \cos L$ and $B = \sqrt{1 - P_1^2 - P_2^2}$. Therefore, the value a_D is:

$$a_D = \frac{1}{2}\rho C_D \frac{A}{m}\frac{\mu}{a}\left(\frac{2\Phi(L)}{B^2} - 1\right) \tag{23}$$

The drag acceleration $\mathbf{a}_{drag}$ is directed along the opposite direction of the velocity vector of the spacecraft and therefore its orientation in the radial-transverse-normal reference frame is defined by the flight path angle γ as:

$$\mathbf{a}_{drag} = \begin{cases} a_r = a_D \sin\gamma \\ a_\theta = a_D \cos\gamma \\ a_h = 0 \end{cases} \tag{24}$$

where γ is:

$$\tan\gamma = \frac{e\sin\theta}{1 + e\cos\theta} \tag{25}$$

The angle γ can be expressed as a function of the equinoctial elements as:

$$\begin{aligned} \sin\gamma &= \frac{P_2 \sin L - P_1 \cos L}{D} \\ \cos\gamma &= \frac{1 + P_1 \sin L + P_2 \cos L}{D} \end{aligned} \tag{26}$$

where $D = \sqrt{1 + P_1^2 + P_2^2 + 2(P_2 \cos L + P_1 \sin L)}$. The three components of the acceleration due to the atmospheric drag can be expressed, using Eqs. (23), (24) and (26) as:

$$\begin{aligned} a_r &= \frac{1}{2}\rho C_D \frac{A}{m}\frac{\mu}{a}\left(\frac{2\Phi(L)}{B^2} - 1\right)\frac{(P_2 \sin L - P_1 \cos L)}{D} \\ a_\theta &= \frac{1}{2}\rho C_D \frac{A}{m}\frac{\mu}{a}\left(\frac{2\Phi(L)}{B^2} - 1\right)\frac{(1 + P_1 \sin L + P_2 \cos L)}{D} \\ a_h &= 0 \end{aligned} \tag{27}$$

By substituting this acceleration in Gauss' planetary equations, the following analytical equations for the variations of the equinoctial elements can be obtained:

$$
\begin{aligned}
a &= a_0 + a_0^2 C_D \frac{A}{m}\left(e_0^2 I_{Drag1} + I_{Drag2}\right) \\
P_1 &= P_{10} + B_0^2 a_0 C_D \frac{A}{m}\left[\sin\left(\Omega_0+\omega_0\right)\left(eI_{Drag3}+I_{Drag5}\right) + \cos\left(\Omega_0+\omega_0\right) I_{Drag4}\right] \\
P_2 &= P_{20} + B_0^2 a_0 C_D \frac{A}{m}\left[\cos\left(\Omega_0+\omega_0\right)\left(eI_{Drag3}+I_{Drag5}\right) - \sin\left(\Omega_0+\omega_0\right) I_{Drag4}\right] \\
Q_1 &= Q_{10} \\
Q_2 &= Q_{20}
\end{aligned}
\tag{28}
$$

where $a_0, P_{10}, P_{20}, Q_{10}$ and Q_{20} are the initial equinoctial elements. I_{Drag1}, I_{Drag2}, I_{Drag3}, I_{Drag4} and I_{Drag5} are:

$$
I_{Drag1} = \int_{\theta_0}^{\theta} \frac{\sin^2\vartheta\sqrt{1+e^2+2e\cos\vartheta}}{(1+e\cos^2\vartheta)^2}\rho(\vartheta)d\vartheta \tag{29}
$$

$$
I_{Drag2} = \int_{\theta_0}^{\theta} \sqrt{1+e^2+2e\cos\vartheta}\rho(\vartheta)d\vartheta \tag{30}
$$

$$
I_{Drag3} = \int_{\theta_0}^{\theta} \frac{\sqrt{1+e^2+2e\cos\vartheta}}{(1+e\cos^2\vartheta)^2}\rho(\vartheta)d\vartheta \tag{31}
$$

$$
I_{Drag4} = \int_{\theta_0}^{\theta} \frac{\sin\vartheta\sqrt{1+e^2+2e\cos\vartheta}}{(1+e\cos^2\vartheta)^2}\rho(\vartheta)d\vartheta \tag{32}
$$

$$
I_{Drag5} = \int_{\theta_0}^{\theta} \frac{\cos\vartheta\sqrt{1+e^2+2e\cos\vartheta}}{(1+e\cos^2\vartheta)^2}\rho(\vartheta)d\vartheta \tag{33}
$$

The atmospheric density ρ is expressed as an expansion in the altitude h of the following form:

$$
\rho\left(\theta\right) = \sum_{j=0}^{N} c_j h(\theta)^j = \sum_{j=0}^{N} c_j \left(\frac{p}{1+e\cos\theta} - R_{\oplus}\right)^j \tag{34}
$$

where p is the orbit parameter, $p = a(1-e^2)$. In order to better approximate the density profile, different value of the coefficients c_j are computed for different ranges of altitude. The altitude is broken down in the following segments: [150, 250] km, [250, 350] km, [350, 500] km, [500, 700] km, [700,

1000] km, [1000, 2000] km, [2000, 3000] km, [3000, 4000] km and [4000, 36,000] km. On each segment a Chebyshev polynomial of order $N = 4$ is used for $\rho(\theta)$:

$$\rho(\theta) = k_0 + k_1 \left(\frac{1}{1+e\cos\theta}\right) + k_2 \left(\frac{1}{1+e\cos\theta}\right)^2 + k_3 \left(\frac{1}{1+e\cos\theta}\right)^3 + \\ + k_4 \left(\frac{1}{1+e\cos\theta}\right)^4$$

where

$$\begin{aligned} k_0 &= c_0 - c_1 R_\oplus + c_2 R_\oplus^2 - c_3 R_\oplus^3 + c_4 R_\oplus^4 \\ k_1 &= c_1 p - 2c_2 p R_\oplus + 3c_3 p R_\oplus^2 - 4c_4 p R_\oplus^3 \\ k_2 &= c_2 p^2 - 3c_3 p^2 R_\oplus + 6c_4 p^2 R_\oplus^2 \\ k_3 &= c_3 p^3 - 4c_4 p^3 R_\oplus \\ k_4 &= c_4 p^4 \end{aligned}$$

The coefficients c_j are obtained by fitting the polynomial expansion to the exponential atmospheric density model in Vallado & McClain (2001). By substituting the previous expression for $\rho(\theta)$ in Eqs (29) to (33) the integrals take the form:

$$I_{Drag-n} = \sum_{j=0}^{j=4} k_n I_{Drag-nj} \qquad n = 1, \ldots 5 \tag{35}$$

The expression of the integrals and their analytical solutions are reported in Appendix A.

In the following, the integral in Eq. (35), is simply added to the effects due to J_2 and low-thrust acceleration. Fig. 10 shows the comparison of numerical and averaged analytical propagation for a propagation of 4 months considering perturbations due to J_2, atmospheric drag and continuous negative tangential acceleration due to a thrust of 0.1 N applied to a 3000 kg spacecraft with initial orbital elements defined in Table 3. For the atmospheric drag, the drag coefficient C_D is set to 2.2 and the area to mass ratio of the spacecraft is assumed to be $A/m = 10^{-2}\mathrm{m}^2/\mathrm{kg}$. The numerical propagation is realized using Matlab *ode113* with integration of the equations of Gauss. The proposed propagation is an example of the deorbiting phase of

Table 3: Initial orbital elements for propagation with J2, atmospheric drag and negative tangential acceleration

a [km]	e	i [deg]	Ω [deg]	ω [deg]
7470	0.01	63.43	10	10

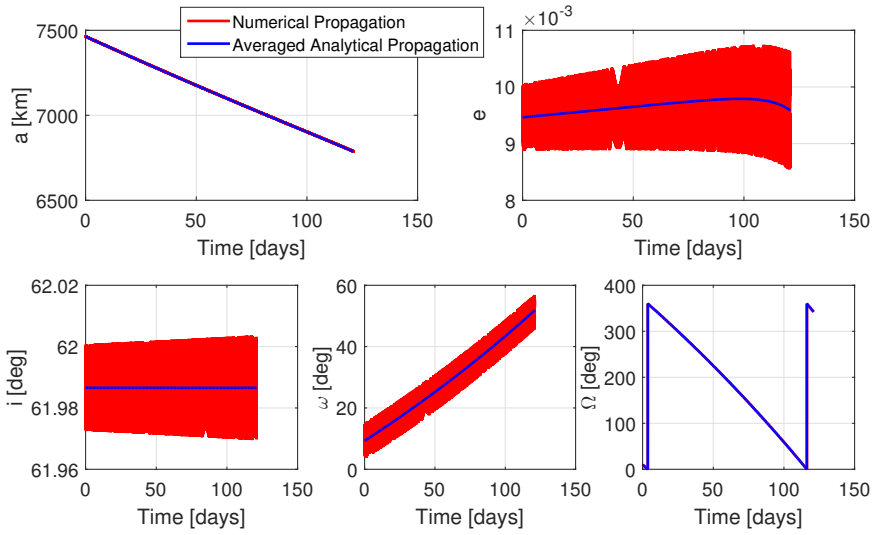

Figure 10: Comparison of averaged analytical and numerical propagation with J_2, atmospheric drag and continuous low-thrust negative tangential acceleration.

the Deorbiting VRP. The results of the averaged analytical propagator are in agreement with those of the numerical propagation.

Particular attention has to be paid when the propagation is realised over longer period of time and at lower altitudes. In this case the coupling of J2 and atmospheric drag requires a corrective term δr to the radial position (Curell (1998)):

$$r = r_{Keplerian} + \delta r \tag{36}$$

where

$$r_{Keplerian} = \frac{r}{1 + e\cos\theta} \tag{37}$$

and

$$\delta r = J_2 \frac{R_\oplus^2}{p} \left\{ \frac{1}{4}\sin^2 i \cos 2\left(\omega + \theta\right) - \left[\frac{1}{2} - \frac{3}{4}\sin^2 i\right] \left[1 + \frac{e\cos\theta}{1+\sqrt{1-e^2}} + \frac{2}{\sqrt{1-e^2}\frac{r}{a}}\right] \right\} \tag{38}$$

The corrective terms δr has to be added to r in Eq. (34). To show the effect of the coupling term a propagation of one year considering J2 and atmospheric drag is realised using the initial orbital elements defined in Table 4, describing a lower altitude orbit than the one in Table 3.

Table 4: Initial orbital elements for one year propagation with J2 and atmospheric drag.

a [km]	e	i [deg]	Ω [deg]	ω [deg]
6978.14	0.03	30	0	30

When the corrective term is not taken into account the averaged analytical propagation gives an error with respect to the numerical propagation, as shown in Fig. 11. When using the corrective term δr for r, however, the results of the averaged analytical propagation coincide with those of the numerical propagation, as shown in Fig. 12. In this case the propagation was realised with numerical integration of Eq. (29) to (33). The numerical integration of these equations slows down the averaged propagator by a factor of at least 6. However, for the purpose of this study, the results obtained are valid without the corrective term, as shown in Fig. 10. This is due to the rapid deorbit of the satellite due to the presence of the low-thrust acceleration, meaning that the coupling effect of J_2 and atmospheric drag is not felt by the satellite. Therefore the integrals reported in Appendix A, that do not include the corrective term δr, can be used.

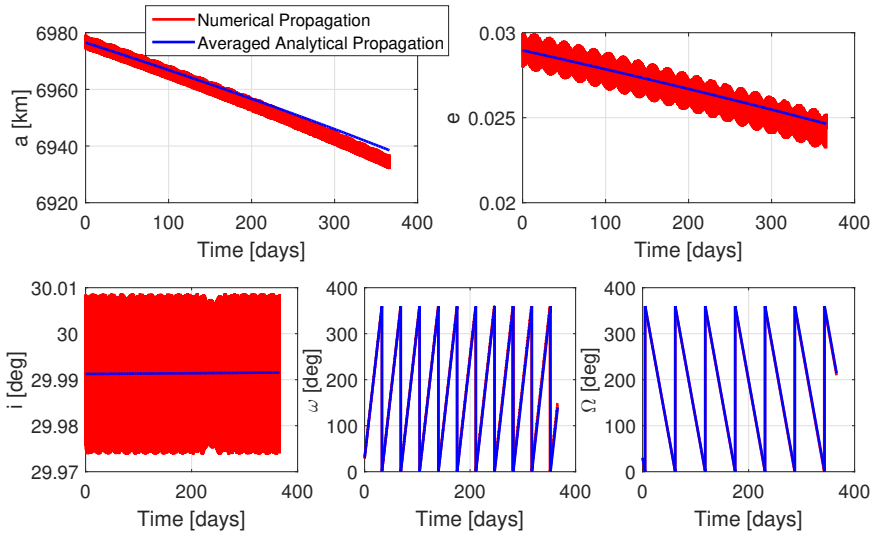

Figure 11: Comparison of averaged analytical and numerical propagation with J2 and atmospheric drag without corrective term for the position.

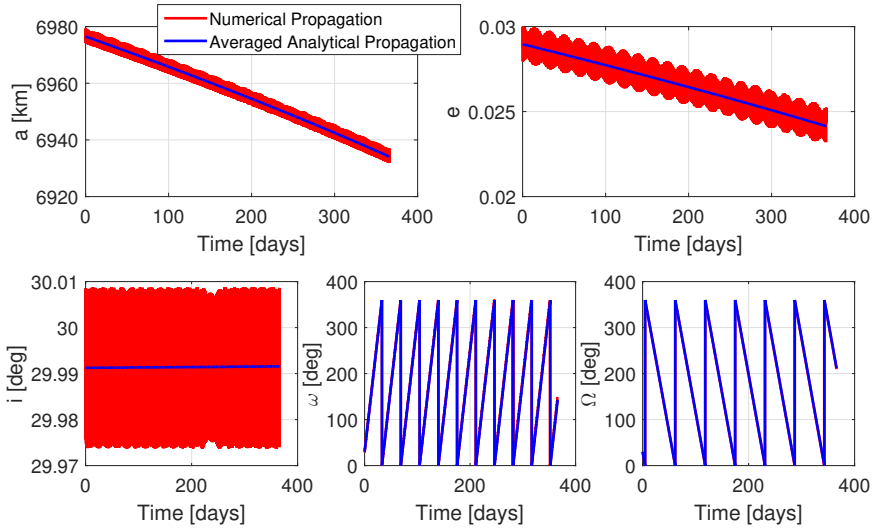

Figure 12: Comparison of averaged analytical and numerical propagation with J2 and atmospheric drag with corrective term for the position.

5.4. Rendezvous strategy

The rendezvous of the chaser with the target object requires imposing a terminal constraint on all the six orbital elements. For a transfer realised in a given time of flight, ToF, the optimisation problems consists in minimising the ΔV required to realise the transfer subject to the terminal constraints:

$$\mathbf{C} = \begin{bmatrix} a_C - a_T \\ e_C - e_T \\ i_C - i_T \\ \Omega_C(t_0 + ToF) - \Omega_T(t_0 + ToF) \\ \omega_C(t_0 + ToF) - \omega_T(t_0 + ToF) \\ \theta_C(t_0 + ToF) - \theta_T(t_0 + ToF) \end{bmatrix} = \mathbf{0} \tag{39}$$

where t_0 is the departure time and the subscripts C and T denote the chaser servicing spacecraft and the target, respectively.

The method we propose to satisfy constraint equations (39) takes advantage of the natural rate of nodal regression and its dependence on the altitude (Pollard, 2000). The total transfer, characterised by a time of flight ToF, is divided into different phases. In the first phase, an optimisation problem is solved in order to satisfy the terminal constraints on e, i and ω, while minimising the propellant consumption in a time $ToF_{e,i,\omega}$.

The second phase is realised in a time of flight $ToF_{a,\Omega} = ToF - ToF_{e,i,\omega}$ and its aim is to correct a and Ω, while keeping the terminal value of i and e and ω constant. It has to be noted that ω is not expected to change much during the transfer because of the inclination of the targets, which is close to the critical value of 63.43 deg. In order to achieve the final desired a and Ω the following strategy, that takes advantage of the natural nodal regression and its dependence on altitude, is used (Chamot & Richard, 2012):

- An optimisation problem is solved in order to minimise the ΔV required to move the spacecraft, in a time of flight T_{t1}, from the orbit attained at time $ToF_{e,i,\omega}$ to an appropriate parking orbit with semimajor axis a_w, while constraining e to be equal to the target's eccentricity e_T. Since this transfer is realised with in-plane thrust only ($\beta = 0$), no change of inclination will take place and therefore no constraint on i is required.
- The spacecraft remains on the parking orbit for an appropriate time $T_{w,\Omega}$.

- An optimisation problem is solved in order to minimise the ΔV required to move the spacecraft, in a time of flight T_{t2}, from the parking orbit to the final orbit with semimajor axis a_T, while constraining e and ω to be equal to e_T and $\omega_T(t_0 + ToF_{e,i,\omega} + T_{t1} + T_{w,\Omega} + T_{t2})$. Since this transfer is realised with in-plane thrust only ($\beta = 0$), no change of inclination will take place and therefore no constraint on i is required. At the end of this transfer the following condition is satisfied:

$$\Omega_C(t_0 + ToF_{e,i,\omega} + ToF_{a,\Omega}) = \Omega_T(t_0 + ToF_{e,i,\omega} + ToF_{a,\Omega}) \quad (40)$$

where $ToF_{a,\Omega}$ corresponds to the sum of transfer times and waiting time:

$$T_{t1} + T_{w,\Omega} + T_{t2} = ToF_{a,\Omega} = ToF - ToF_{e,i,\omega} \quad (41)$$

This strategy requires the computation of four parameters: T_{t1}, a_w, $T_{w,\Omega}$ and T_{t2}. Hence, four equations are required to solve the problem. The first one derives directly from the available time, Eq. (41). The second equations is derived from Edelbaum theory for the required ΔV for a transfer between circular orbits (Edelbaum (1961)). This equation applies here because of the small eccentricity of the orbits of the targets. By denoting the semimajor axis of the chaser the end of the first phase with $a_{C(e,i,\omega)}$, the time to realise the transfer to the parking orbit can be computed as the ratio between the required ΔV and the spacecraft acceleration:

$$T_{t1} = \frac{k\sqrt{V_{C(e,i,\omega)}^2 + V_w^2 - 2V_{C(e,i,\omega)}V_w}}{\varepsilon} \quad (42)$$

where $V_{C(e,i,\omega)}$ is the circular velocity on the orbit of radius $a_{C(e,i,\omega)}$ and V_w is the circular velocity on an orbit of radius a_w. The quantity ε is the acceleration of the electric engine and the factor $k = 1.5$ is used to accommodate the extra time required to satisfy the constraints on e and ω. Similarly:

$$T_{t2} = \frac{k\sqrt{V_T^2 + V_w^2 - 2V_T V_w}}{\varepsilon} \quad (43)$$

where now V_T is the velocity on a circular orbit of radius equal to the semimajor axis of the target object. The forth equation is the matching condition on Ω at the end of the transfer:

$$\Omega_T(t_0) + \dot{\Omega}_T(T_{t1} + T_{t2} + T_{w,\Omega}) = \Omega_C(t_0) + \dot{\Omega}_{t1}T_{t1} + \dot{\Omega}_w T_{w,\Omega} + \dot{\Omega}_{t2}T_{t2} \quad (44)$$

In Eq. (44) $\dot{\Omega}_T$ is the drift of the right ascension of the target orbit and $\dot{\Omega}_{t1}$ and $\dot{\Omega}_{t2}$ are the drifts of the right ascensions of the transfers to and from the parking orbit. The drift $\dot{\Omega}$ changes during these two transfers because of the variation of semimajor axis but it can be approximated to be constant by using a mean semimajor axis $a_{t1} = \frac{a_{C(e,i,\omega)}+a_w}{2}$ for the transfer to the parking orbit and a mean semimajor axis $a_{t2} = \frac{a_w+a_T}{2}$ for the transfer from the parking orbit to the target orbit. Eqs (41) to (44) allow to compute T_{t1}, a_w, $T_{w,\Omega}$ and T_{t2} required for the change of Ω.

5.4.1. Orbital phasing

One underlying assumption in the estimation of the ΔV is that the transfer requires a long spiral in which the variation of orbital elements over a complete revolution is small. In this case, the orbital elements over the first revolution of the spiral will be very similar to the orbital elements of the departure orbit. Likewise, the orbital elements over the last revolution of the spiral will be very similar to the orbital elements of the target orbit. Furthermore, the initial and final true anomalies can change by at most 2π, which corresponds to equal or less than the orbital period of the departure, or target, orbit. Hence, a change of initial or final phase angle to match the initial and terminal conditions will have little effect on the overall spiral and thus on the total ΔV.

An example is reported hereafter to show that the variation in ΔV when changing the departure true anomaly and reducing the time of flight by less than one orbital period is negligible. Let us consider as an example, the transfer from object 39012 to object 39016, realised with a time of flight of 44 days. Table 5 show the ΔV required for the transfer, for different initial masses of the spacecraft and the three cases: (1) $t_w = 0$, $ToF = 44$ days; (2) $t_w = 40$ min, $ToF = 44$ days; (3) $t_w = 43$ min, $ToF = 44$ days - 43 min, where t_w is a waiting time on the departure orbit, before starting the transfer, that causes a change of the initial phase angle.

Given its negligible effect on the ΔV and ToF, the phasing will not be considered when estimating the cost of the transfers.

5.5. Problem transcription

For the Deorbiting TSP strategy, the chaser rendezvous with each object using the strategy described in Sec. 5.4. During the optimisation process the drag perturbation is not included in the analytical propagator because the effect of the drag is negligible at the considered altitudes. As an example

Table 5: ΔV required for the transfer from object 39012 to object 39016 for different initial masses of the spacecraft, departure times and times of flight.

m [kg]	ToF = 44 days $t_w = 0$ min	ToF = 44 days $t_w = 40$ min	ToF = 44 days - 43 min $t_w = 43$ min
800	0.0836	0.0836	0.0838
1000	0.0856	0.0856	0.0858
1200	0.0886	0.0886	0.0858
1400	0.0947	0.0947	0.0931
1600	0.1110	0.1110	0.1101

of the Deorbiting TSP, Figures 13 shows the variation of orbital elements during the transfer from object 40342 to object 40338, realised in 42 days.

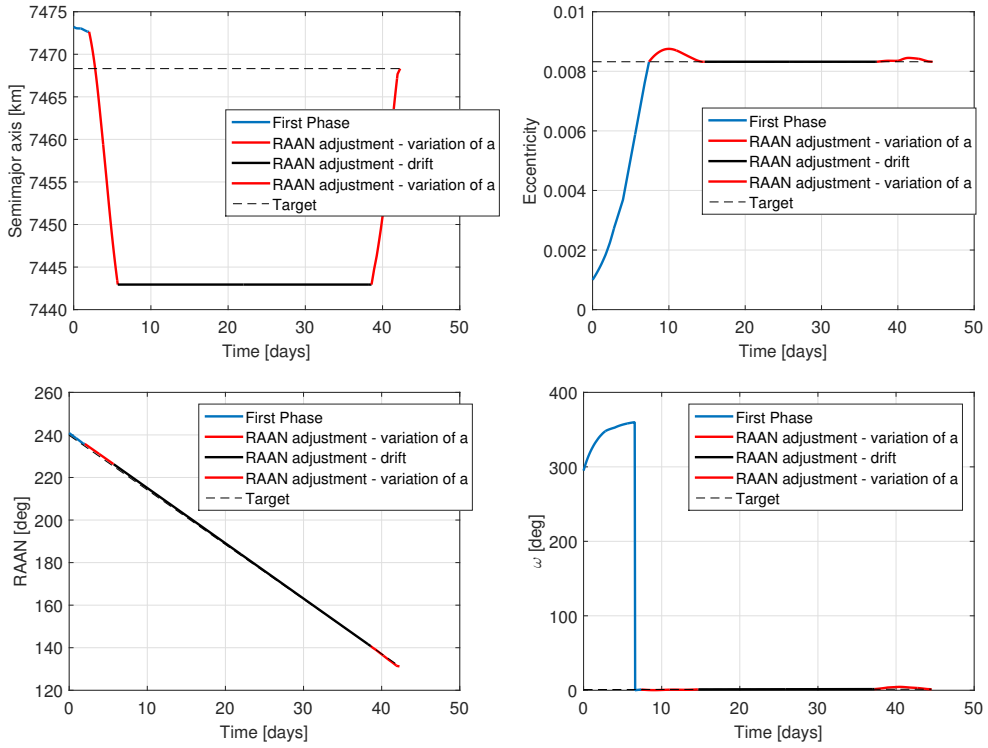

Figure 13: Orbital element variation of the chaser and of the target object 40338 during the transfer from spacecraft 40342 to 40338.

For the Deorbiting VRP, the following transfer model is assumed. Con-

sidering a situation in which the chaser has already realised rendezvous and docking with one of the target objects, the total transfer from one target to another consists in the following phases:

- The chaser de-orbits the target object by applying a constant negative tangential thrust over all its orbit, until it reaches a perigee of 300 km altitude. Once this disposal orbit has been reached, the servicing spacecraft disengages with the target.
- The chaser increase its semimajor axis by applying a constant positive tangential thrust, until it reaches the semimajor axis of the next target object
- The chaser rendezvous with the next target object using the strategy described in Sec. 5.4

The deorbiting and orbit raising phases are computed using the averaged analytical propagator described in Sec. 5.4 and considering both J_2 and drag perturbations. As an example, Fig. 14 shows the variation of perigee altitude of the chaser (grabbing object 36413 during the deorbiting phase) and the subsequent orbit raising phase. The total time required is 180 days. The shorter orbit raising time is due to the fact that, when the perigee reaches 300 km, the servicing spacecraft dispose of the target. The orbit raising phase is, therefore, realised with a lower mass, resulting in an increased acceleration. Fig. 14 shows also the variation of RAAN of the servicing spacecraft during the deorbit and orbit raising phases and the variation of right ascension of the next target object, 39011. The right ascension of the two objects at the end of the orbit raising phase is very close, resulting in a reduced transfer time to the target object.

5.6. Optimisation method

A direct method based on a single-shooting, direct collocation method is used. The MATLAB fmincon-sqp algorithm is used to solve the problem. Four nodes and linear interpolation are used to model the variation of the control variables in the optimisation of the first transfer of the rendezvous strategy when e, i and ω are modified. From four to eight nodes are used for the optimisation of the transfer to and from the parking orbit in order to adjust Ω.

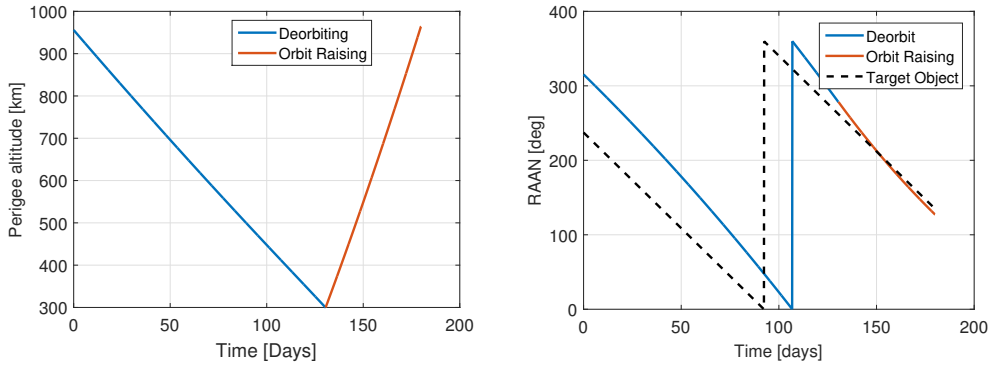

Figure 14: Variation of the perigee altitude for the servicing spacecraft during deorbit of object 36413 and orbit raising to the semimajor axis of target object 39011.

5.6.1. Low-thrust transfer surrogate model

In order to reduce the computational burden in the process of the identification of the optimal sequence of targets, a surrogate model of the low-thrust transfer model is used by the Physarum algorithm to evaluate the cost to link two nodes (Sec. 4), (Zuiani & Vasile (2012)).

The surrogate was generated before the optimisation using a database of pre-computed transfers between pairs of departure and target orbits. The surrogate model yields the value of the ΔV for a given combination of mass and time of flight. For this study, the Matlab Toolbox DACE (Design and Analysis of Computer Experiment) has been used to construct a Kriging-based surrogate of the ΔV (Lophaven et al., 2002). As an example, Fig. 15 shows the surrogate model for the transfer from object 36414 to object 36417.

6. Mission definition

For this study, an electric propulsion engine providing 0.1 N of thrust and characterised by a specific impulse I_{sp} of 1600 s is considered. The wet mass of the servicing spacecraft, without the mass of the deorbiting kits, is 1000 kg. Each serviced target is assumed to have a mass of 2000 kg [1].

[1] http://astronautix.com/c/changzheng4c.html

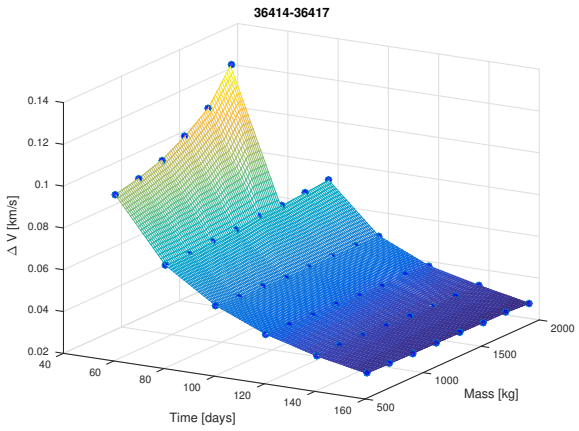

Figure 15: Surrogate model for the computation of ΔV for the transfer 36414-36417

For the Deorbiting TSP, 10 de-orbit kits of 175 kg are assumed to be on board the servicing spacecraft, resulting in a total initial mass of 2750 kg. The mass of 175 kg has been estimated considering the propellant required to reduce the perigee of the orbit of all the considered targets to 300 km. Assuming that the de-orbiting kit is activated at the apogee of the orbit of the target, the ΔV_{DK} required to reduce the perigee altitude to $h_{pD} = 300$ km is:

$$\Delta V_{DK} = \sqrt{2\frac{\mu}{r_a} - \frac{\mu}{a}} - \sqrt{2\frac{\mu}{r_a} - \frac{\mu}{a_D}} \tag{45}$$

where a is the semimajor axis of the satellite to be deorbited (Table 1), r_a is its apogee radius and $a_D = (r_a + r_{pD})/2$, where $r_{pD} = h_{pD} + R_\oplus$.

Assuming a specific impulse of the deorbiting kit of $I_{sp} = 303.5$ s (Zandbergen (2013)) and a structural mass fraction equal to 0.2 (to include also the mass of the attaching mechanism of the de-orbit kit), the higher mass of de-orbit kit for all the objects in Table 1 is 175 kg.

It is assumed that at 300 km the effect of the drag is relevant enough to cause the re-entry of the object. For the objects in Table 1, a perigee altitude of 300 km causes the object to re-enter naturally in a time that goes from a minimum of 541 days to a maximum of 654 days. Introducing a lower altitude, corresponding, for example, to a controlled re-entry is also possible and would simply increase the mass of all the de-orbiting kits without affecting the overall strategy.

A 175 kg drop is modeled after each transfer to simulate the attachment of the de-orbit kit to the target. The propellant mass resulting from the

transfer is also subtracted from the current mass.

6.1. Physarum algorithm settings

In addition to the Physarum algorithms parameters m, ρ, GF, N_{agents}, p_{ram}, r_{ini}, $k_{exploration}$ and λ introduced in Sec. 4, additional quantities need to be defined. These additional parameters are the set of targets $S_s = \{S_1, S_2, \ldots, S_{N_P}\}$ (Table 1), the mission start epoch, t_{start}, the maximum mission time, T_{max}, the lower and upper boundaries on the time of flight ToF_{min} and ToF_{max} for each leg connecting two targets i and j, the time spent at the target to dock and install the de-orbiting kit, $t_{servicing}$, and the maximum allowed change of velocity ΔV_{max}. Another important parameter is the maximum number of function calls, $Feval_{max}$, where a function call corresponds to the evaluation of one arc. The values of the parameters of the Physarum algorithm, together with the additional problem parameters used in this study are reported in Table 6.

Table 6: Setting parameters

m	5×10^{-3}
ρ	10^{-4}
GF	5×10^{-3}
N_{agents}	40
$N_{Generation}$	40
p_{ram}	0.7
λ	1
r_{ini}	1
$k_{exploration}$	2
$Feval_{max}$	1×10^5
S_s	All elements in Table 1
t_{start}	30 May 2015
T_{max}	365 days
ToF_{min}	1 day
ToF_{max}	60 days for the De-Orbit kit strategy
	185 days for the Spiral Down&Up strategy
$t_{servicing}$	7 days
ΔV_{max}	2.0 km/s

7. Results

This section presents the results obtained for each of the two proposed ADR strategies. For each one of the two strategies, the Physarum solver was run on 25 different instances of the optimisation problem. Each instance uses one of the 25 targets in Table 1 as the starting point of the sequence of targeted objects. Each optimisation was repeated 50 times, given the stochastic nature of the Pysarum solver.

7.1. Deorbiting TSP

Figure 16 shows the results obtained when considering different possible initial targets for the 50 runs of the Physarum solver. The x-axis shows the NORAD ID of the first target in the sequence and the y-axis the total ΔV (left) and time of flight (right) required for the entire mission. Each dot corresponds to one of the 50 solutions.

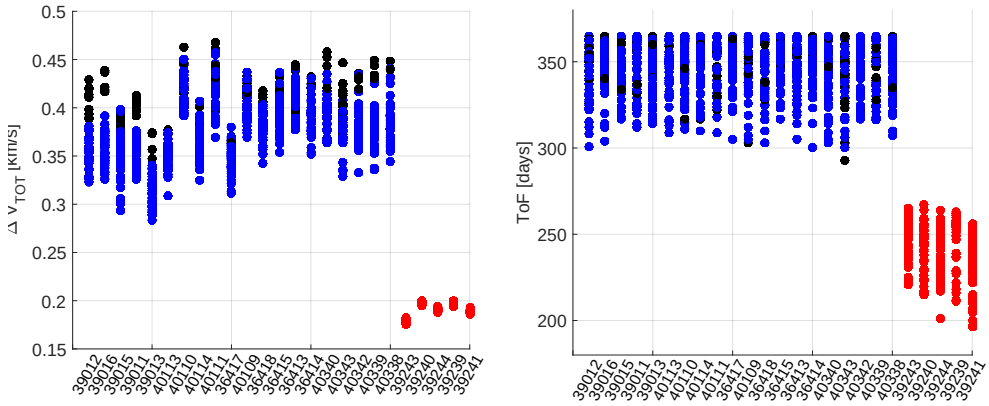

Figure 16: ΔV of 50 runs of the Physarum solver for the Deorbiting TSP, using different initial objects (as shown on the x axis). Black dots represent solution with 10 de-orbited objects, blue dots solutions with 9 de-orbited objects and red dots solutions with 5 de-orbited objects.

Figure 16 shows that the solver found solutions with 10 or 9 de-orbited objects in most of the cases but could find only sequences with a maximum of 5 de-orbited objects if the first object is 39243, 39240, 39244, 39239 or 39241. This is due to the value of the right ascension of these objects, extremely different from the right ascension of the others (see Table 1). This means that a transfer from these targets to any other target in Table 1 requires longer time of flight.

The solution characterised by the maximum number of visited objects (10) and lower ΔV is reported in Table 7. Ten objects, identified in Table 7 by their NORAD ID, can be removed in less than one year. The mass m_0 is the mass at the beginning of each transfer and m_f the mass at the end of each transfer. The drop in mass at the beginning of each transfer is due to the attachment of the de-orbit kit. ToF represents the time of flight required to realise each transfer. The total time of the mission, considering a servicing time of 7 days for each object, is 365 days.

Table 7: Sequence of satellite for Deorbiting TSP.

	Departure Object	Arrival Object	ΔV [km/s]	ToF [days]	m_0 [kg]	m_f [kg]
1	39013	39011	0.010	51.00	2575.00	2398.35
2	39011	39012	0.004	10.00	2398.35	2222.81
3	39012	39016	0.093	27.00	2222.81	2034.60
4	39016	40342	0.044	31.00	2034.60	1853.95
5	40342	40340	0.013	32.00	1853.95	1677.44
6	40340	40339	0.024	43.00	1677.44	1499.85
7	40339	40338	0.003	2.00	1499.85	1324.58
8	40338	40343	0.114	52.00	1324.58	1139.98
9	40343	39015	0.042	54.00	1139.98	961.90
Total	-	-	0.3470	302	-	-

Information about the variability of the results obtained by the Physarum solver are given in Table 8. The first column shows the target used as root for the generation of the tree; the second column shows the maximum number of de-orbited targets starting from that root; the third column reports the number of runs (out of the 50) that return a number of de-orbited targets equal to the maximum number in column two; column four reports the number of unique sequences among the solutions with number of de-orbited targets equal to the maximum number; ΔV_{min} is the minimum cost of the solutions with maximum number of de-orbited targets and the last column reports the number of solutions with same sequence of visited targets as the one of with ΔV_{min}. The result relative to Table 7 is shown in bold. The sequence of targets reported in Table 7 is found 2 times by the Physarum solver, once with ΔV equal to 0.3470 km/s and total time of flight of 365

days (Table 7) and once with a ΔV of 0.3730 km/s and 334 days of time of flight.

Table 8: Analysis of the results given by the Physarum solver for the Deorbiting TSP.

Root	Max. num. objects	Num. sol. max. num. objects	Unique seq. max. obj.	ΔV_{min} [km/s]	Num. sol. same seq. ΔV_{min}
39012	10	9/50	4	0.3889	5
39016	10	5/50	3	0.4163	3
39015	10	10/50	6	0.3666	1
39011	10	9/50	3	0.3920	5
39013	**10**	**4/50**	**3**	**0.3470**	**2**
40113	10	2/50	2	0.3719	1
40110	10	6/50	4	0.4050	3
40114	10	6/50	4	0.3720	2
40111	10	7/50	5	0.3992	3
36417	10	2/50	2	0.3639	1
40109	10	8/50	6	0.4065	1
36418	10	5/50	4	0.3956	1
36415	10	5/50	3	0.4037	1
36413	10	5/50	4	0.3969	2
36414	10	7/50	4	0.3943	1
40340	10	4/50	3	0.4200	2
40343	10	21/50	9	0.3724	4
40342	10	5/50	3	0.4190	3
40339	10	6/50	4	0.4282	2
40338	10	3/50	2	0.4255	2
39243	5	50/50	1	0.1755	50
39240	5	50/50	2	0.1951	34
39244	5	50/50	3	0.1882	26
39239	5	50/50	2	0.1939	31
39241	5	50/50	2	0.1865	42

The average run time per generation of the optimiser on one TSP instance using 40 agents is 2 minutes on an Intel(R) Core(TM) i7-3770 CPU 3.4GHz with 8GB RAM with the code implemented in Matlab.

7.2. Deorbiting VRP

Figure 17 shows the results obtained when considering different possible initial targets for the Deorbiting VRP and 50 runs of the solver. The x-axis shows the NORAD ID of the first target in the sequence and the y-axis the total ΔV and time of flight required for the entire mission.

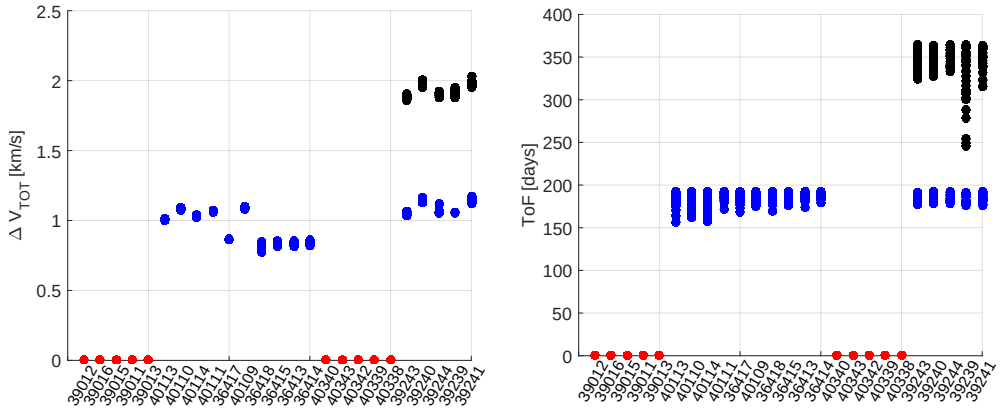

Figure 17: ΔV of 50 runs of the Physarum solver for the Deorbiting VRP, with different initial object in the sequence (as shown on the x axis). Black dots represent solution with 3 serviced objects, blue dots solutions with 2 serviced objects and red dots represents solution with 1 serviced objects.

The solution characterised by the maximum number of de-orbited targets and lower ΔV for the Deorbiting VRP ADR is reported in Table 9. In this Table ToF represents the time required to deorbit the initial target, raise the orbit to the semimajor axis of the next target and then adjust all the other orbital elements.

Table 9: Sequence of satellite for the Deorbiting VRP strategy.

	Departure Object	Arrival Object	ΔV [km/s]	ToF [days]	m_0 [hours]	m_f [kg]	[kg]
1	39243	36413	1.049	163.00	3000.00	2888.62	
2	36413	39015	0.809	183.00	2888.62	2801.66	
Total	-	-	1.8571	353	-	-	

The deorbiting of a target from the selected altitude region and the subsequent orbit raising to the next target takes a considerable amount of time,

making this strategy not viable to remove 5 to 10 targets per year. These results are in agreement with Virgili & Krag (2009), who found that 5 objects per year can not be actively de-orbited by grabbing and moving them to a given disposal orbit. Information about the variability of the results obtained with the Physarum solver are given in Table 10. The results relative to Table 9 are shown in bold. In this case the Physarum solver finds 5 solutions with sequence equal to the one reported in Table 10.

For the Deorbiting VRP the run time is dependent upon the target used as root of the decision graph. The maximum run time per generation for 40 agents is 11 minutes on an Intel(R) Core(TM) i7-3770 CPU 3.4GHz with 8GB RAM with the code implemented in Matlab.

8. Conclusions

In this paper, two Active Debris Removal strategies were analysed: Deorbiting TSP and VRP. In the Deorbiting TSP strategy a servicing spacecraft, equipped with low-thrust propulsion engine, attach a de-orbit device to each target to be removed; in the Deorbiting VRP strategy the servicing spacecraft grab the targets and deorbit them using low-thrust propulsion. Targets in LEO with altitude in the 800-1400 km range were considered in this analysis.

In order to find the optimal sequence of targets to be serviced (with the objective of maximising the number of de-orbited objects and minimising the propellant consumption), an innovative incremental planning and scheduling optimisation algorithm have been used. In order to reduce the computational burden, the planning and scheduling algorithm was used in conjunction with the use of a surrogate model of the low-thrust transfer model.

This planning approach provided, per run, 1600 solutions in approximately 80 minutes for the Deorbiting TSP and in a maximum time of 7 hours for the Deorbiting VRP. On the Deorbiting TSP, out of the 1600 solutions, the planner could consistently find sequences with 10 objects, together with a large number of sequences with 9 objects or less. For the Deorbiting VRP, solutions fulfilling the one year constraint were limited to 3 targets.

This paper has shown that the Deorbiting TSP strategy is the most effective ADR method, given the time constraint of 1 year for the mission time. Up to 10 targets per year can be removed with this strategy. On the contrary, the time required by the Deorbiting VRP strategy to deorbit one single target makes it an unfeasible option. This is in agreement with what found by Virgili & Krag (2009). Moreover the Deorbiting TSP strategy is also less

Table 10: Information about the variability of the results of the Physarum solver for the Spiral Deorbiting VRP strategy.

Root	Max. num. objects	Num. sol. max. num. objects	Unique seq. max. obj.	ΔV_{min} [km/s]	Num. sol. same seq. ΔV_{min}
39012	1	50/50	1	-	-
39016	1	50/50	1	-	-
39015	1	50/50	1	-	-
39011	1	50/50	1	-	-
39013	1	50/50	1	-	-
40113	2	50/50	1	1.0026	50
40110	2	50/50	3	1.0710	48
40114	2	50/50	1	1.0219	50
40111	2	50/50	2	1.0592	34
36417	2	50/50	3	0.8581	12
40109	2	50/50	4	1.0837	42
36418	2	50/50	2	0.7748	48
36415	2	50/50	2	0.8172	39
36413	2	50/50	3	0.8118	36
36414	2	50/50	4	0.8190	21
40340	1	50/50	1	-	-
40343	1	50/50	1	-	-
40342	1	50/50	1	-	-
40339	1	50/50	1	-	-
40338	1	50/50	1	-	-
39243	**3**	**29/50**	**9**	**1.8571**	**5**
39240	3	26/50	4	1.9513	5
39244	3	26/50	7	1.8766	13
39239	3	41/50	4	1.8753	17
39241	3	28/50	8	1.9513	5

risky because the servicing spacecraft spends a shorter time in contact with the non-cooperative target and is not subjected to perturbation experienced during the deorbiting phase.

To be noted that the De-orbiting TSP strategy analysed in this paper considers identical de-orbiting kits for each satellite and a cost function that does not depend on the mass of the de-orbiting kit. If the mass of the de-

orbiting kit was included in the cost function the planner would yield also the optimal distribution of de-orbiting kits for a given scenario. This will be the subject of a future investigation.

Further work will look into the evaluation of the impact of the relaxation of some of the constraint parameters such as the maximum time of flight or the maximum mission time on the number of feasible solutions, in particular for the Deorbiting VRP strategy. In addition, single and multi-servicing spacecraft mission options will be considered and the same strategies will be applied to a different groups of targets.

Acknowledgements

This research was partially supported by Aibus Defence and Space and the Marie Curie FP7-PEOPLE-2012-ITN Stardust. The authors would like to thank Mr Stephen Kemble for his support and contribution.

References

Adamatzky, A., Martnez, G. J., Chapa-Vergara, S. V., Asomoza-Palacio, R., & Stephens, C. R., Approximating Mexican highways with slime mould, Natural Computing, 10(3), 1195-1214. 2011.

Battin, R. H., An introduction to the mathematics and methods of astrodynamics AIAA, 1999.

Bombardelli, C., & Pelaez, J., Ion beam shepherd for contactless space debris removal. Journal of guidance, control, and dynamics, 34(3), 916-920, 2011.

Braun, V., Lpken, A., Flegel, S., Gelhaus, J., Mckel, M., Kebschull, C., Wiedemann, C., Vrsmann, P.. Active debris removal of multiple priority targets. Advances in Space Research, 51(9), 1638-1648, 2013.

Castronuovo, M. M., Active space debris removal A preliminary mission analysis and design. Acta Astronautica, 69(9), 848-859, 2011.

Cefola, P. J., Long, A. C., & Holloway Jr, G.. The long-term prediction of artificial satellite orbits, AIAA 12th Aerospace Sciences Meeting, Washington D.C., January-February 1974.

Chamot, B., & Richard, M., Mission and system architecture design for active removal of rocket bodies in low earth orbit, Masters thesis, Massachusetts Institute of Technology, US, August 2012.

Chobotov, V. A., Orbital Mechanics, American Institute of Aeronautics and Astronautics. Inc., Reston, VA, 20. 2002.

Curell, P. C., GRACE Orbit Analysis Tool and parametric analysis, Master's thesis, University of Texas at Austin, 1998.

Edelbaum, T. N., Propulsion requirements for controllable satellites. ARS Journal, 31(8), 1079-1089, 1961.

Gil, A., Segura, J., & Temme, N. M., Numerical methods for special functions. Siam, 2007.

D. S. Hickey & L. A. Noriega, Insights into Information Processing by the Single Cell Slime Mold Physarum Polycephalum, UKACC Control Conference, 2008.

Hildreth, S. A., and Arnold, A., Threats to US National Security Interests in Space: Orbital Debris Mitigation and Removal, Library of Congress Washington DC Congressional Research Service, January 2014.

Hoots, F. R., & Roehrich, R. L., Spacetrack report no. 3. Colorado Springs CO: Air Force Aerospace Defence Command, 1-3, 1980.

Jones, Donald R., A taxonomy of global optimization methods based on response surfaces, Journal of global optimization, no. 4, 345-383, 2001.

Kessler, D. J., Johnson, N. L., Liou, J. C., & Matney, M., The kessler syndrome: implications to future space operations, Advances in the Astronautical Sciences, 137(8), 2010.

Inter-Agency Space Debris Coordination Committee Space Debris Mitigation Guidelines, 45th Session of the Scientific and Technical Subcommittee, United Nations Committee on the Peaceful Uses of Outer Space, 2007

Liou, J. C., & Johnson, N. L., Instability of the present LEO satellite populations, Advances in Space Research, 41(7), 1046-1053, 2008.

Lophaven, S. N., Nielsen, H. B., & Sndergaard, J. DACE - A MATLAB Kriging Toolbox, 2002.

Masi, L., & Vasile, M., A multidirectional Physarum solver for the automated design of space trajectories, IEEE Congress In Evolutionary Computation (CEC), 2992-2999. July 2014.

Monismith, D. R., & Mayfield, B. E. , Slime mold as a model for numerical optimization. IEEE Swarm Intelligence Symposium. 2008.

Nakagaki, T., Yamada, H., and Tth, ., Intelligence: Maze-solving by an amoeboid organism, Nature, 407(6803), 470-470, 2000

Olympio, J. T., & Frouvelle, N., Space debris selection and optimal guidance for removal in the SSO with low-thrust propulsion. Acta Astronautica, 99, 263-275, 2014.

Ortiz Gmez, N., Walker S.J., Eddy Currents applied to De-tumbling of Space Debris: Analysis and Validation of Approximate Proposed Methods', Acta Astronautica, Volume 114, Pages 34-53, April 2015.

Peterson, G. E., Target identification and Delta-V sizing for active debris removal and improved tracking campaigns. In 23rd International Symposium on Spaceflight Dynamics, Pasadena, California, October 2012.

Pollard, J. E., Simplified Analysis of Low-Thrust Orbital Maneuvers, AEROSPACE CORP EL SEGUNDO CA TECHNOLOGY OPERATIONS, (No. TR-2000 (8565)-10) 2000.

Rossi, A., & Valsecchi, G. B., Collision risk against space debris in Earth orbits, Celestial Mechanics and Dynamical Astronomy, 95(1-4), 345-356, 2006.

Rossi, A., Valsecchi, G. B., & Alessi, E. M., The Criticality of Spacecraft Index, Advances in Space Research, 2015.

Ruggiero, A., Pergola, P., Marcuccio, S., & Andrenucci, M., Low-Thrust Maneuvers for the Efficient Correction of Orbital Elements. 32nd International Electric Propulsion Conference (pp. 1-13). September 2011.

Stuart J., Howell K., Wilson R., Application of multi-agent coordination methods to the design of space debris mitigation tours, Advances in Space Research, May 2015.

Tero, A., Yumiki, K., Kobayashi, R., Saigusa, T., Nakagaki, R., Flow-Network Adaptation in Physarum Amoebae, Theory in Biosciences, Volume 127, 2, 98-94, 2008.

Tero., A., Kobayashi., K., & Nakagaki, T., Physarum solver: a biologically inspired method of road-network navigation, Physica A: Statistical Mechanics and its Applications 363.1, 115-119, 2006.

Vallado, D. A., & McClain, W. D., Fundamentals of astrodynamics and applications, Springer Science & Business Media, 2001.

Vasile, M., Romero Martin, J. M., Masi, L., Minisci, E., Epenoy, R., Martinot, V., Fontdecaba, Baig J., Incremental planning of multi-gravity assist trajectories,Acta Astronautica Volume 115, October/November 2015, Pages 407421.

Vasile, M., & Becerra, V. M., Computational intelligence in aerospace sciences, American Institute of Aeronautics and Astronautics, 2014.

Vasile, M., Maddock, C., & Saunders, C., Orbital debris removal with solar concentrators. In 61st International Astronautical Congress, IAC 2010.

Virgili, B. B., & Krag, H., Strategies for active removal in LEO. EMR, 2(5.0), 5-0, 2009.

Wormnes, K., Le Letty, R., Summerer, L., Schonenborg, R., Dubois-Matra, O., Luraschi, E., & Delaval, J. , ESA technologies for space debris remediation, 6th IAASS Conference: Safety is Not an Option (pp. 3-4). April 2013

Zuiani, F., & Vasile, M., Preliminary design of debris removal missions by means of simplified models for low-thrust, many-revolution transfers. International Journal of Aerospace Engineering, 2012.

Zuiani, F., & Vasile, M., Extended analytical formulas for the perturbed Keplerian motion under a constant control acceleration. Celestial Mechanics and Dynamical Astronomy, 121(3), 275-300, 2015.

Kumar, K., Ortiz Gómez, N., Jankovic, M., Romero Martin, J.M., Topputo, F., Walker, S., Kirchner, F., Vasile, M., Agora: Mission to demonstrate technologies to actively remove Ariane rocket bodies, 66st International Astronautical Congress, IAC 2015.

Zandbergen, I., Some typical solid propellant rocket motors, Memorandum, TU Delft, December 2013.

Appendix A. Analytical Integrals

Appendix A.1. I_{Drag-1}

$$I_{Drag-1} = k_0 I_{Drag-10} + k_1 I_{Drag-11} + k_2 I_{Drag-12} + k_3 I_{Drag-13} + k_4 I_{Drag-14} \quad \text{(A.1)}$$

$$\begin{aligned} I_{Drag10} = \int_{\theta_0}^{\theta} \frac{\sin\vartheta\sqrt{1+e^2+2e\cos\vartheta}}{(1+e\cos\theta)^2}d\vartheta = \Bigg[& \frac{3+e^2}{e^2(1+e)}F\left(\frac{\vartheta}{2}, \frac{4e}{(1+e)^2}\right) + \\ & -\frac{3(1+e)}{e^2}E\left(\frac{\vartheta}{2}, \frac{4e}{(1+e)^2}\right) + \frac{1}{e^2}\log\left(\frac{\sqrt{1+e^2+2e\cos\vartheta}+e\sin\vartheta}{\sqrt{1+e^2+2e\cos\vartheta}-e\sin\vartheta}\right) + \\ & +\frac{\sin\vartheta\sqrt{1+e^2+2e\cos\vartheta}}{e(1+e\cos\vartheta)}\Bigg]_{\theta_0}^{\theta} \end{aligned}$$

$$\begin{aligned} I_{Drag11} = \int_{\theta_0}^{\theta} \frac{\sin\vartheta\sqrt{1+e^2+2e\cos\vartheta}}{(1+e\cos\vartheta)^3}d\vartheta = \Bigg\{ & -\frac{1}{e^2(1+e)}E\left[\arcsin\left(\cos\frac{\vartheta}{2}\right), -\frac{4e}{(1-e)^2}\right] + \\ & + \frac{2}{e^2(1-e)}F\left[\arcsin\left(\cos\frac{\vartheta}{2}\right), -\frac{4e}{(1-e)^2}\right] + \\ & -\frac{(1+e)^2}{e^2(1-e^2)}\Pi\left[-\frac{2e}{1-e}, \arcsin\left(\cos\frac{\vartheta}{2}\right), -\frac{4e}{(1-e)^2}\right] - \frac{\sin\vartheta(1+e^2+2e\cos\vartheta)^{3/2}}{2e(1-e^2)(1+e\cos\vartheta)^2}\Bigg\}_{\theta_0}^{\theta} \end{aligned}$$

where

$$\begin{aligned} \Pi\left[-\frac{2e}{1-e}, \arcsin\left(\cos\frac{\vartheta}{2}\right), -\frac{4e}{(1-e)^2}\right] = & \frac{1}{1+e}F\left[\arcsin\left(\cos\frac{\vartheta}{2}\right), -\frac{4e}{(1-e)^2}\right] + \\ & \frac{1}{4}\frac{(1-e)}{(1+e)}\log\left[\frac{\left(\tan(\vartheta/2)\sqrt{1+e^2+2e\cos\vartheta}+(1+e)\right)\left((1-e)\tan(\vartheta/2)-\sqrt{1+e^2+2e\cos\vartheta}\right)}{\left(\tan(\vartheta/2)\sqrt{1+e^2+2e\cos\vartheta}-(1+e)\right)\left((1-e)\tan(\vartheta/2)+\sqrt{1+e^2+2e\cos\vartheta}\right)}\right] \end{aligned}$$

$$I_{Drag-12} = \int_{\theta_0}^{\theta} \frac{\sin\vartheta\sqrt{1+e^2+2e\cos\vartheta}}{(1+e\cos\vartheta)^4}d\vartheta = \\ \left\{ -\frac{(e^4-2e^3+2e^2-2e+1)}{3e^2(1-e)^3(1+e)^2}E\left[\arcsin\left(\cos\frac{\vartheta}{2}\right), -\frac{4e}{(1-e)^2}\right] + \right. \\ + \frac{(e^4-2e^2+1)}{3e^2(1-e)^3(1+e)^2}F\left[\arcsin\left(\cos\frac{\vartheta}{2}\right), -\frac{4e}{(1-e)^2}\right] + \\ \left. -\frac{e\sin\vartheta A_{12}}{3e^2(1-e)^2(1+e)^2(1+e\cos\vartheta)^3\sqrt{1+e^2+2e\cos\vartheta}} \right\}_{\theta_0}^{\theta]}$$

where

$$A_{12} = (2e^5+2e^3)\cos^3\vartheta + (e^6+4e^4+7e^2)\cos^2\vartheta + (-e^5+8e^3+5e)\cos\vartheta + \\ + (-e^6+e^4+3e^2+1)$$

$$I_{Drag-13} = \int_{\theta}^{\theta_0} \frac{\sin\vartheta\sqrt{1+e^2+2e\cos\vartheta}}{(1+e\cos\vartheta)^5}d\vartheta = \\ \left\{ -\frac{(e^4-2e^3+2e^2-2e+1)}{3e^2(1-e)^4(1+e)^3}E\left[\arcsin\left(\cos\frac{\vartheta}{2}\right), -\frac{4e}{(1-e)^2}\right] + \right. \\ + \frac{(e^4-2e^2+1)}{12e^2(1-e)^4(1+e)^3}F\left[\arcsin\left(\cos\frac{\vartheta}{2}\right), -\frac{4e}{(1-e)^2}\right] + \\ + \frac{(e^5+e^4-2e^3-2e^2+e+1)}{4e^2(1-e)^4(1+e)^3}\Pi\left[-\frac{2e}{1-e}, \arcsin\left(\cos\frac{\vartheta}{2}\right), -\frac{4e}{(1-e)^2}\right] \\ \left. -\frac{e\sin\vartheta A_{13}}{24e^2(1-e)^3(1+e)^3(1+e\cos\vartheta)^4\sqrt{1+e^2+2e\cos\vartheta}} \right\}_{\theta_0}^{\theta}$$

where

$$A_{13} = (16e^6+16e^4)\cos^4\vartheta + (2e^7+60e^5+66e^3)\cos^3\vartheta + (-3e^8+15e^6+75e^4+105e^2)\cos^2\vartheta + \\ (10e^7-24e^5+82e^3+60e)\cos\vartheta + (6e^8-11e^6-e^4+27e^2+11)$$

$$I_{Drag14} = \int_{\theta_0}^{\theta} \frac{\sin\vartheta\sqrt{1+e^2+2e\cos\vartheta}}{(1+e\cos\vartheta)^6}d\vartheta =$$
$$\left\{-\frac{(2e^6-4e^5+5e^4-6e^3+10e^2-14e+7)}{15e^2(1-e)^5(1+e)^4}E\left[\arcsin\left(\cos\frac{\vartheta}{2}\right),-\frac{4e}{(1-e)^2}\right]+\right.$$
$$+\frac{(4e^6-9e^4+6e^2-1)}{30e^2(1-e)^5(1+e)^4}F\left[\arcsin\left(\cos\frac{\vartheta}{2}\right),-\frac{4e}{(1-e)^2}\right]+$$
$$+\frac{1}{2e^2(1-e)^3(1+e)}\Pi\left[-\frac{2e}{1-e},\arcsin\left(\cos\frac{\vartheta}{2}\right),-\frac{4e}{(1-e)^2}\right]$$
$$\left.-\frac{\sin\vartheta A_{14}}{60e(1-e)^4(1+e)^4(1+e\cos\vartheta)^5\sqrt{1+e^2+2e\cos\vartheta}}\right\}_{\theta_0}^{\theta}$$

where

$$A_{14} = (192e^9+24e^7+56e^5)\cos^5\vartheta+(8e^{10}+62e^8+132e^6+278e^4)\cos^4\vartheta+$$
$$+(29e^9+97e^7+279e^5+555e^3)\cos^3\vartheta+$$
$$+(4e^{10}+23e^8+103e^6+269e^4+561e^2)\cos^2\vartheta+$$
$$+(-22e^9+111e^7-97e^5+229e^3+259e)\cos\vartheta+$$
$$+(-12e^{10}+34e^8-11e^6-29e^4+71e^2+143)$$

Appendix A.2. I_{Drag-2}

$$I_{Drag-2} = k_0 I_{Drag-20}+k_1 I_{Drag-21}+k_2 I_{Drag-22}+k_3 I_{Drag-23}+k_4 I_{Drag-24} \quad \text{(A.2)}$$

$$I_{Drag-20} = \int_{\theta_0}^{\theta}\sqrt{1+e^2+2e\cos\vartheta}d\vartheta = 2(1+e)\left[E\left(\frac{\vartheta}{2},\frac{4e}{(1+e)^2}\right)\right]_{\theta_0}^{\theta}$$

$$I_{Drag-21} = \int\frac{\sqrt{1+e^2+2e\cos\theta}}{(1+e\cos\theta)}d\theta = \frac{2}{(1+e)}\left[2F\left(\frac{\theta}{2},\frac{4e}{(1+e)^2}\right)+\right.$$
$$\left.+(-1+e)\Pi\left(\frac{2e}{1+e},\frac{\theta}{2},\frac{4e}{(1+e)^2}\right)\right]$$

$$I_{Drag-22} = \int_{\theta_0}^{\theta} \frac{\sqrt{1+e^2+2e\cos\vartheta}}{(1+e\cos\vartheta)^2} d\vartheta = I_{Drag-40}$$

$$\begin{aligned} I_{Drag-23} = \int_{\theta_0}^{\theta} \frac{\sqrt{1+e^2+2e\cos\vartheta}}{(1+e\cos\vartheta)^3} d\vartheta = \\ \left\{ -\frac{1}{(1-e)(1+e)^2} E\left[\arcsin\left(\cos\frac{\vartheta}{2}\right), -\frac{4e}{(1-e)^2}\right] + \right. \\ -\frac{1}{(1-e)^2}\Pi\left[-\frac{2e}{1-e}, \arcsin\left(\cos\frac{\vartheta}{2}\right), -\frac{4e}{(1-e)^2}\right] + \\ \left. -\frac{e\sin\vartheta(2e^2+8e\cos\theta+4e^2\cos^2\vartheta-e^4+3)}{2(1-e)^2(1+e)^2\sqrt{1+e^2+2e\cos\vartheta}(1+e\cos\vartheta)^2} \right\}_{\theta_0}^{\theta} \end{aligned}$$

$$\begin{aligned} I_{Drag-24} = \int_{\theta_0}^{\theta} \frac{\sqrt{1+e^2+2e\cos\vartheta}}{(1+e\cos\vartheta)^4} d\vartheta = \\ \left\{ -\frac{2(1+e^2)}{3(1-e)^2(1+e)^3} E\left[\arcsin\left(\cos\frac{\vartheta}{2}\right), -\frac{4e}{(1-e)^2}\right] + \right. \\ +\frac{2}{3(1-e)^2(1+e)} F\left[\arcsin\left(\cos\frac{\vartheta}{2}\right), -\frac{4e}{(1-e)^2}\right] + \\ -\frac{2}{(1-e)^3(1+e)}\Pi\left[-\frac{2e}{1-e}, \arcsin\left(\cos\frac{\vartheta}{2}\right), -\frac{4e}{(1-e)^2}\right] + \\ \left. +\frac{\sin\vartheta e A_{24}\sqrt{1+e^2+2e\cos\vartheta}}{3(e^6-3e^4+3e^2-2)(1+e\cos\vartheta)^3} \right\}_{\theta_0}^{\theta} \end{aligned}$$

where

$$A_{24} = (2e^4+2e^2)\cos^2\vartheta + (2e^3+6e)\cos\vartheta + (e^4-2e^2+5)$$

Appendix A.3. I_{Drag-3}

$$I_{Drag-3} = k_0 I_{Drag-30} + k_1 I_{Drag-31} + k_2 I_{Drag-32} + k_3 I_{Drag-33} + k_4 I_{Drag-34} \quad \text{(A.3)}$$

$$I_{Drag-30} = \int_{\theta_0}^{\theta} \frac{\sqrt{1+e^2+2e\cos\vartheta}}{(1+e\cos\vartheta)^2} d\vartheta = \left[\frac{1}{(1-e)} E\left(\frac{\vartheta}{2}, \frac{4e}{(1+e)^2}\right) + \frac{1}{(1+e)} F\left(\frac{\vartheta}{2}, \frac{4e}{(1+e)^2}\right) + -\frac{e\sin\vartheta\sqrt{1+e^2+2e\cos\vartheta}}{(1-e^2)(1+e\cos\vartheta)} \right]_{\theta_0}^{\theta}$$

$$I_{Drag-31} = \int_{\theta_0}^{\theta} \frac{\sqrt{1+e^2+2e\cos\vartheta}}{(1+e\cos\vartheta)^3} d\vartheta = I_{Drag-23}$$

$$I_{Drag-32} = \int_{\theta_0}^{\theta} \frac{\sqrt{1+e^2+2e\cos\vartheta}}{(1+e\cos\vartheta)^4} d\vartheta = I_{Drag-24}$$

$$I_{Drag-33} = \int_{\theta_0}^{\theta} \frac{\sqrt{1+e^2+2e\cos\vartheta}}{(1+e\cos\vartheta)^5} d\vartheta = \left\{ -\frac{2e^2}{(1-e)^3(1+e)^4} E\left[\arcsin\left(\cos\frac{\vartheta}{2}\right), -\frac{4e}{(1-e)^2}\right] + + \frac{5}{4(1-e)^3(1+e)^2} F\left[\arcsin\left(\cos\frac{\vartheta}{2}\right), -\frac{4e}{(1-e)^2}\right] + -\frac{(3e^2+13)}{4(1-e)^4(1+e)^2} \Pi\left[-\frac{2e}{1-e}, \arcsin\left(\cos\frac{\vartheta}{2}\right), -\frac{4e}{(1-e)^2}\right] + -\frac{e\sin\vartheta A_{33}\sqrt{1+e^2+2e\cos\vartheta}}{8(e^8-4e^6+6e^4-4e^2+1)(1+e\cos\vartheta)^4} \right\}_{\theta_0}^{\theta}$$

where

$$A_{33} = 16e^5\cos^3\vartheta + (-3e^6+46e^4+5e^2)\cos^2\vartheta + (-2e^5+36e^3+14e)\cos\vartheta + (-2e^6+7e^4+11)$$

$$I_{Drag-34} = \int_{\theta_0}^{\theta} \frac{\sqrt{1+e^2+2e\cos\vartheta}}{(1+e\cos\theta)^6} d\vartheta$$
$$\left\{ -\frac{(8e^4+57e^2-17)}{15(1-e)^4(1+e)^5} E\left[\arcsin\left(\cos\frac{\vartheta}{2}\right), -\frac{4e}{(1-e)^2}\right] + \right.$$
$$+\frac{4(2e^2+7)}{15(1-e)^4(1+e)^3} F\left[\arcsin\left(\cos\frac{\vartheta}{2}\right), -\frac{4e}{(1-e)^2}\right] +$$
$$\left. -\frac{(3e^2+5)}{(1-e)^5(1+e)^3} \Pi\left[-\frac{2e}{1-e}, \arcsin\left(\cos\frac{\vartheta}{2}\right), -\frac{4e}{(1-e)^2}\right] \right\}_{\theta_0}^{\theta}$$

Appendix A.4. I_{Drag-4}

$$I_{Drag-4} = k_0 I_{Drag-40} + k_1 I_{Drag-41} + k_2 I_{Drag-42} + k_3 I_{Drag-43} + k_4 I_{Drag-44} \quad \text{(A.4)}$$

$$I_{Drag-40} = \int_{\theta_0}^{\theta} \frac{\sin\vartheta\sqrt{1+e^2+2e\cos\vartheta}}{(1+e\cos\theta)^2} d\vartheta = \left[-\frac{2}{e\sqrt{1-e^2}} \arctan\left(\sqrt{\frac{1+e^2+2e\cos\vartheta}{1-e^2}}\right) + \right.$$
$$\left. + \frac{\sqrt{1+e^2+2e\cos\theta}}{e(1+e\cos\vartheta)} \right]_{\theta_0}^{\theta}$$

$$I_{Drag-41} = \int_{\theta_0}^{\theta} \frac{\sin\vartheta\sqrt{1+e^2+2e\cos\vartheta}}{(1+e\cos\vartheta)^3} d\vartheta = \left[-\frac{1}{e\sqrt{(1-e^2)^3}} \arctan\left(\sqrt{\frac{1+e^2+2e\cos\vartheta}{1-e^2}}\right) + \right.$$
$$\left. - \frac{(e+\cos\vartheta)\sqrt{1+e^2+2e\cos\vartheta}}{2(1-e^2)(1+e\cos\vartheta)^2} \right]_{\theta_0}^{\theta}$$

$$I_{Drag-42} = \int_{\theta_0}^{\theta} \frac{\sin\vartheta\sqrt{1+e^2+2e\cos\vartheta}}{(1+e\cos\vartheta)^4} d\vartheta = \left[-\frac{1}{e\sqrt{(1-e^2)^5}} \arctan\left(\sqrt{\frac{1+e^2+2e\cos\vartheta}{1-e^2}}\right) + \right.$$
$$\left. - \frac{(1+2e^2+3e\cos\vartheta)(-2+e^2-e\cos\vartheta)\sqrt{1+e^2+2e\cos\vartheta}}{6e(1-e^2)^2(1+e\cos\vartheta)^3} \right]_{\theta_0}^{\theta}$$

$$I_{Drag-43} = \int_{\theta_0}^{\theta} \frac{\sin\vartheta\sqrt{1+e^2+2e\cos\vartheta}}{(1+e\cos\vartheta)^5}d\vartheta = \left\{ -\frac{5}{4e\sqrt{(1-e^2)^7}} \arctan\left(\sqrt{\frac{1+e^2+2e\cos\theta}{1-e^2}}\right) + \right.$$
$$\left. + \frac{\sqrt{1+e^2+2e\cos\theta}}{24e(1+e\cos\vartheta)^4}\left[6 - \frac{2(1+e\cos\vartheta)}{(1-e^2)} - \frac{5(1+e\cos\vartheta)^2}{(1-e^2)^2} - \frac{15(1+e\cos\vartheta)^3}{(1-e^2)^3}\right]\right\}_{\theta_0}^{\theta}$$

$$I_{Drag-44} = \int \frac{\sin\theta\sqrt{1+e^2+2e\cos\theta}}{(1+e\cos\theta)^6}d\theta = \left\{ -\frac{7}{4e\sqrt{(1-e^2)^9}} \arctan\left(\sqrt{\frac{1+e^2+2e\cos\vartheta}{1-e^2}}\right) + \right.$$
$$- \frac{\sqrt{1+e^2+2e\cos\vartheta}}{120e(1+e\cos\vartheta)^5}\left[-24 + \frac{6(1+e\cos\vartheta)}{1-e^2} + \frac{14(1+e\cos\vartheta)^2}{(1-e^2)^2} + \frac{35(1+e\cos\vartheta)^3}{(1-e^2)^3} + \right.$$
$$\left.\left. + \frac{105(1+e\cos\vartheta)^4}{(1-e^2)^4}\right]\right\}_{\theta_0}^{\theta}$$

Appendix A.5. I_{Drag-5}

$$I_{Drag-5} = k_0 I_{Drag-50} + k_1 I_{Drag-51} + k_2 I_{Drag-52} + k_3 I_{Drag-53} + k_4 I_{Drag-54} \quad \text{(A.5)}$$

$$I_{Drag-50} = \int_{\theta_0}^{\theta} \frac{\cos\vartheta\sqrt{1+e^2+2e\cos\vartheta}}{(1+e\cos\vartheta)^2}d\vartheta = \left\{ \frac{1}{e(1+e)}E\left[\arcsin\left(\cos\frac{\vartheta}{2}\right), -\frac{4e}{(1-e)^2}\right] + \right.$$
$$- \frac{3}{e(1-e)}F\left[\arcsin\left(\cos\frac{\vartheta}{2}\right), -\frac{4e}{(1-e)^2}\right] +$$
$$\left. + \frac{2(1+e)}{e(1-e)}\Pi\left[-\frac{2e}{1-e}, \arcsin\left(\cos\frac{\vartheta}{2}\right), -\frac{4e}{(1-e)^2}\right] + \frac{\sin\vartheta\sqrt{1+e^2+2e\cos\theta}}{(1-e)(1+e)(1+e\cos\vartheta)}\right\}_{\theta_0}^{\theta}$$

$$I_{Drag-51} = \int_{\theta_0}^{\theta} \frac{\cos\vartheta\sqrt{1+e^2+2e\cos\vartheta}}{(1+e\cos\vartheta)^3}d\vartheta = \left\{ \frac{e}{(1-e)(1+e)^2}E\left[\arcsin\left(\cos\frac{\vartheta}{2}\right), -\frac{4e}{(1-e)^2}\right] + \right.$$
$$- \frac{1}{e(1-e)}F\left[\arcsin\left(\cos\frac{\vartheta}{2}\right), -\frac{4e}{(1-e)^2}\right] +$$
$$+ \frac{1}{e(1-e)^2}\Pi\left[-\frac{2e}{1-e}, \arcsin\left(\cos\frac{\vartheta}{2}\right), -\frac{4e}{(1-e)^2}\right] +$$
$$\left. + \frac{\sin\vartheta A_{51}}{2(1-e)^2(1+e)^2(1+e\cos\vartheta)^2\sqrt{1+e^2+2e\cos\vartheta}}\right\}_{\theta_0}^{\theta}$$

where

$$A_{51} = (4e^4)\cos^2\vartheta + (2e^5 + 4e^3 + 2e)\cos\vartheta + (e^4 + 2e^2 + 1)$$

$$I_{Drag-52} = \int_{\theta_0}^{\theta} \frac{\cos\vartheta\sqrt{1+e^2+2e\cos\vartheta}}{(1+e\cos\vartheta)^4} d\vartheta =$$
$$\left\{ \frac{(5e^4 - 10e^3 + 4e^2 + 2e - 1)}{3e(1-e)^4(1+e)^3} E\left[\arcsin\left(\cos\frac{\theta}{2}\right), -\frac{4e}{(1-e)^2}\right] + \right.$$
$$- \frac{2}{3e(1-e)^2(1+e)} F\left[\arcsin\left(\cos\frac{\vartheta}{2}\right), -\frac{4e}{(1-e)^2}\right] +$$
$$+ \frac{(1+e^2)}{e(1-e)^3(1+e)} \Pi\left[-\frac{2e}{1-e}, \arcsin\left(\cos\frac{\vartheta}{2}\right), -\frac{4e}{(1-e)^2}\right] +$$
$$\left. + \frac{\sin\vartheta A_{52}}{6(1-e)^3(1+e)^3(1+e\cos\vartheta)^3\sqrt{1+e^2+2e\cos\vartheta}} \right\}_{\vartheta_0}^{\vartheta}$$

where

$$A_{52} = (20e^5 - 4e^3)\cos^3\vartheta + (4e^6 + 52e^4 - 8e^2)\cos^2\vartheta + (-3e^7 + 17e^5 + 35e^3 - e)\cos\vartheta +$$
$$+ (-e^6 + 7$$

$$I_{Drag-53} = \int_{\theta_0}^{\theta} \frac{\cos\vartheta\sqrt{1+e^2+2e\cos\vartheta}}{(1+e\cos\vartheta)^5} d\vartheta =$$
$$\left\{ \frac{2(e^4 + 3e^2 - 1)}{3e(1-e)^3(1+e)^4} E\left[\arcsin\left(\cos\frac{\vartheta}{2}\right), -\frac{4e}{(1-e)^2}\right] + \right.$$
$$- \frac{(8e^2+7)}{12e(1-e)^3(1+e)^2} F\left[\arcsin\left(\cos\frac{\vartheta}{2}\right), -\frac{4e}{(1-e)^2}\right] +$$
$$+ \frac{(11e^2+5)}{4e(1-e)^4(1+e)^3} \Pi\left[-\frac{2e}{1-e}, \arcsin\left(\cos\frac{\vartheta}{2}\right), -\frac{4e}{(1-e)^2}\right] +$$
$$\left. + \frac{\sin\theta A_{53}\sqrt{1+e^2+2e\cos\theta}}{24(e^8 - 4e^6 + 6e^4 - 4e^2 + 1)(1+e\cos\theta)^4} \right\}_{\theta_0}^{\theta}$$

where

$$A_{53} = (16e^7 + 48e^5 - 16e^3)\cos^3\vartheta + (23e^6 + 170e^4 - 49e^2)\cos^2\vartheta +$$
$$+ (8e^7 - 14e^5 + 196e^3 - 46e)\cos\vartheta + +(2e^6 - 3e^4 + 56e^2 - 7)$$

$$I_{Drag-54} = \int_{\theta_0}^{\theta} \frac{\cos\vartheta\sqrt{1+e^2+2e\cos\vartheta}}{(1+e\cos\vartheta)^6}d\vartheta =$$
$$\left\{ \frac{(38e^4+27e^2-17)}{15e(1-e)^4(1+e)^5}E\left[\arcsin\left(\cos\frac{\vartheta}{2}\right), -\frac{4e}{(1-e)^2}\right] + \right.$$
$$-\frac{(107e^2+37)}{60e(1-e)^4(1+e)^3}F\left[\arcsin\left(\cos\frac{\vartheta}{2}\right), -\frac{4e}{(1-e)^2}\right] +$$
$$+\frac{(3e^4+22e^2+7)}{4e(1-e)^5(1+e)^3}\Pi\left[-\frac{2e}{1-e}, \arcsin\left(\cos\frac{\vartheta}{2}\right), -\frac{4e}{(1-e)^2}\right] +$$
$$\left. -\frac{\sin\vartheta A_{54}\sqrt{1+e^2+2e\cos\vartheta}}{120(e^{10}-5e^8+10e^6-10e^4+5e^2-1)(1+e\cos\vartheta)^5} \right\}_{\theta_0}^{\theta}$$

where

$$A_{54} = (304e^8+216e^6-136e^4)\cos^4\vartheta + (-45e^9+1083e^7+1073e^5-575e^3)\cos^3\vartheta +$$
$$+ (-43e^8+1245e^6+2007e^4-905e^2)\cos^2\vartheta +$$
$$+ (-30e^9+121e^7+421e^5+1635e^3-611e)\cos\vartheta +$$
$$+ (-6e^8+23e^6+99e^4+389e^2-121)$$